Check for updates

JGR Solid Earth

RESEARCH ARTICLE
10.1029/2026JB034515

High-Resolution Body-Wave Tomography of Kīlauea's Summit Magma Storage System From a Dense Passive and Active Source Experiment

Guoqing Lin[1], Steven Roecker[2], Roger Denlinger[3], Dan O'Connell[4], Ninfa Bennington[5], Elizabeth Vinarski[1], Ashton Flinders[5], and Matthew M. Haney[6]

[1]Rosenstiel School of Marine, Atmospheric, and Earth Science, University of Miami, Miami, FL, USA, [2]Department of Earth and Environmental Sciences, Rensselaer Polytechnic Institute, Troy, NY, USA, [3]U.S. Geological Survey, Cascades Volcano Observatory, Vancouver, WA, USA, [4]U.S. Geological Survey, Evergreen, CO, USA, [5]U.S. Geological Survey, Hawaiian Volcano Observatory, Hilo, HI, USA, [6]U.S. Geological Survey, Alaska Volcano Observatory, Anchorage, AK, USA

Abstract Imaging magma storage beneath active calderas requires resolving crustal structure at scales comparable to those of individual reservoirs. To identify potential reservoirs beneath Kīlauea, Hawai'i, we conducted a hybrid seismic experiment at its summit for 37 days in 2023 that combined more than 1,800 three-component nodal seismometers with 396 vibroseis source positions, yielding about 15 million *P*- and *S*-wave arrivals. Joint inversion of earthquake and active-source travel times yields three-dimensional models of V_p, V_s, and V_p/V_s within the upper ~4 km beneath the summit relative to mean sea level, parameterized on a 500 m grid, within which the resolution tests demonstrate recovery of sub-kilometer to kilometer-scale structure. The models delineate two principal magma storage regions beneath Halema'uma'u and the south caldera, each on the order of 2 km across. Both reservoirs are expressed as localized zones of reduced V_s and moderately reduced V_p with locally elevated V_p/V_s at depths of 1–3 km below sea level. The anomalies are laterally distinct at shallow levels but appear to merge within a broader zone of reduced velocities at depth. Surrounding higher-velocity domains likely represent mechanically stronger intrusive complexes that confine magma storage. Spatial correspondence between seismic velocity anomalies and independently modeled geodetic deformation sources supports the interpretation that the imaged structures represent magma storage regions. These results demonstrate that dense nodal arrays combined with hybrid passive-active tomography can resolve reservoir-scale structure at active volcanoes and provide an improved framework for interpreting magma storage and transport beneath Kīlauea.

Plain Language Summary We used earthquake and controlled-source vibrations recorded by a dense network of small seismic sensors to create detailed images of the subsurface beneath the summit of Kīlauea. These images show that magma beneath the summit is stored in two regions. One reservoir lies beneath Halema'uma'u crater and is characterized by reduced shear-wave speeds at depths of about 1–3 km, consistent with hot, fractured rock that may contain magma and volcanic gases. A second reservoir lies beneath the south caldera, is more confined, and is characterized by reduced seismic velocities, consistent with magma storage. Although the two reservoirs are laterally separated at shallow depths, our results suggest that they may be linked at greater depth within a broader zone of reduced seismic velocities. The surrounding higher-velocity rock likely acts as a mechanical boundary that helps confine magma and influence how it moves beneath the summit. The seismic patterns agree with independent measurements of ground deformation, increasing confidence that the imaged features represent real magma storage regions. By resolving structures at the sub-kilometer to kilometer scale, this study improves our understanding of how magma is stored and transferred beneath Kīlauea and illustrates an approach applicable to other active volcanoes.

Key Points:

- Joint active and passive-source tomography images the upper ~4 km beneath Kīlauea summit on a 500 m grid, with sub-km to km-scale recovery
- The model reveals two shallow magma storage regions beneath Halema'uma'u and the south caldera
- Low V_s and locally high V_p/V_s align with the recent deformation pattern, supporting the interpretation of magma storage and transport

Supporting Information:

Supporting Information may be found in the online version of this article.

Correspondence to:

G. Lin,
glin@miami.edu

Citation:

Lin, G., Roecker, S., Denlinger, R., O'Connell, D., Bennington, N., Vinarski, E., et al. (2026). High-resolution body-wave tomography of Kīlauea's summit magma storage system from a dense passive and active source experiment. *Journal of Geophysical Research: Solid Earth*, *131*, e2026JB034515. https://doi.org/10.1029/2026JB034515

Received 8 APR 2026
Accepted 2 OCT 2026

Author Contributions:

Conceptualization: Guoqing Lin, Steven Roecker, Roger Denlinger, Dan O'Connell
Data curation: Guoqing Lin, Steven Roecker, Dan O'Connell
Formal analysis: Guoqing Lin
Funding acquisition: Guoqing Lin, Steven Roecker, Roger Denlinger
Investigation: Guoqing Lin
Methodology: Guoqing Lin

© 2026 The Author(s). Journal of Geophysical Research: Solid Earth published by Wiley Periodicals LLC on behalf of American Geophysical Union. This is an open access article under the terms of the Creative Commons Attribution-NonCommercial-NoDerivs License, which permits use and distribution in any medium, provided the original work is properly cited, the use is non-commercial and no modifications or adaptations are made.

1. Introduction

Kīlauea, the most persistently active basaltic volcano on Earth, has long served as the premier natural laboratory for investigating magma generation, transport, and storage in basaltic systems. Its frequent eruptions, near-continuous summit activity, and exceptionally dense geophysical and geological monitoring record have made Kīlauea central to advances in volcanology and solid Earth geophysics. Continuous observations of seismicity, deformation, gas emissions, and eruptive behavior have enabled the development and testing of physical models

Project administration: Guoqing Lin, Roger Denlinger
Resources: Guoqing Lin
Supervision: Guoqing Lin
Validation: Guoqing Lin, Roger Denlinger
Visualization: Guoqing Lin
Writing – original draft: Guoqing Lin
Writing – review & editing: Steven Roecker, Roger Denlinger, Dan O'Connell, Ninfa Bennington, Elizabeth Vinarski, Ashton Flinders, Matthew M. Haney

for magma plumbing systems that are difficult to constrain at less active volcanoes. As a result, conceptual models developed at Kīlauea have often informed interpretations of basaltic volcanoes worldwide.

Prior to 2018, decades of seismological, geodetic, geological, and petrological investigations led to a broadly accepted conceptual model of the summit magma system (e.g., Cervelli & Miklius, 2003; Eaton & Murata, 1960; Okubo et al., 1997; Poland et al., 2014; Ryan, 1988), in which shallow magma reservoirs beneath the summit caldera fed eruptions and intrusions along the East and Southwest Rift Zones. Geodetic observations spanning leveling, electronic distance measurement, tilt, interferometric synthetic aperture radar (InSAR), and continuous Global Positioning System (GPS) documented repeated summit inflation and deflation cycles associated with magma accumulation and withdrawal (e.g., Baker & Amelung, 2012, 2015; Cervelli & Miklius, 2003; Delaney et al., 1990; Dzurisin et al., 1984; Montgomery-Brown et al., 2010; Owen et al., 2000; Segall et al., 2001). In particular, InSAR measurements provided spatially continuous constraints on summit deformation at Kīlauea that complemented ground-based geodetic networks and helped resolve the geometry of shallow deformation sources beneath the caldera (e.g., Baker & Amelung, 2012, 2015). In parallel, seismicity patterns delineated rift-zone conduits, ring-fault structures, and fault-controlled magma pathways extending away from the summit (e.g., Klein et al., 1987; Lin, Shearer, et al., 2014; Matoza et al., 2013; Okubo et al., 1997; Syracuse et al., 2010). Despite this progress, fundamental aspects of the summit system, including the total volume of shallow magma storage, the geometry and connectivity of individual reservoirs, and their physical state, remained incompletely constrained (e.g., Okubo & Wolfe, 2008; Poland et al., 2014). In particular, the degree to which summit reservoirs were vertically connected, laterally segmented, or mechanically isolated from one another remained uncertain.

The 2018 Lower East Rift Zone eruption and the accompanying summit caldera collapse fundamentally challenged these preexisting models. Rapid drainage of magma from the summit into the rift zone, coupled with progressive subsidence and structural failure of the caldera floor, demonstrated that shallow magma storage was both more extensive and more efficiently connected to the rift system than previously inferred (Anderson et al., 2019; Denlinger et al., 2024; Lin & Okubo, 2020; Neal et al., 2019; Patrick et al., 2020). Subsequent analyses further suggested that magma transport beneath Hawai'i may be organized within a complex deep magmatic system, including a mantle sill complex at depths of 36–43 km that may be connected to Kīlauea and Mauna Loa (Wilding et al., 2023). These observations underscore the multiscale connectivity of the Hawaiian magmatic system and highlight the need for improved constraints on the three-dimensional (3-D) shallow structure of the summit region.

Seismic imaging has played a central role in efforts to characterize Kīlauea's magmatic architecture. Early body-wave tomography studies identified broad regions of reduced seismic velocity beneath the summit and rift zones, establishing the existence of a shallow summit magma complex and rift-related low-velocity structure (e.g., Crosson & Koyanagi, 1979; Dawson et al., 1999; Okubo et al., 1997; Rowan & Clayton, 1993; Thurber, 1984). Subsequent investigations using expanded data sets and improved inversion strategies refined these images and better constrained the depth extent of rift- and summit-related anomalies, including evidence for deeper magma bodies beneath the East Rift Zone (e.g., J. Got et al., 2006; J. L. Got et al., 2008; Haslinger et al., 2001; Monteiller et al., 2005; Park et al., 2007, 2009). Island-scale and summit-focused 3-D body-wave tomography that incorporated waveform cross-correlation relocation and joint inversion of *P*- and *S*-wave information demonstrated that shallow low-velocity structure beneath Kīlauea is spatially complex and strongly heterogeneous, and highlighted the importance of explicitly accounting for strong lateral heterogeneity when locating earthquakes and interpreting magma-related anomalies (Lin, Amelung, et al., 2014; Lin, Shearer, et al., 2014).

More recent regional-scale body-wave and ambient-noise tomography studies have imaged large low-velocity anomalies beneath the summit and East Rift Zone that were interpreted as interconnected magma pathways extending from shallow to mid-crustal depths. Ambient-noise surface-wave tomography has provided laterally continuous constraints on shallow shear-wave velocity structure beneath the summit and rift zones of Kīlauea (Wei et al., 2023). Complementary attenuation and velocity-ratio analyses further showed that regions of low velocity beneath Kīlauea are commonly associated with high attenuation and anomalous ratios of compressional-wave velocity (V_p) to shear-wave velocity (V_s), V_p/V_s, consistent with elevated temperatures, partial melt, and volatile-rich conditions in the shallow crust (Lin, Amelung, et al., 2015; Lin, Shearer, et al., 2015). Time-dependent seismic velocity monitoring has also demonstrated that summit velocities evolve in response to pressurization, intrusion, and withdrawal (Lin & Shearer, 2021; Wu et al., 2025).

21699356, 2026, 10, Downloaded from https://agupubs.onlinelibrary.wiley.com/doi/10.1029/2026JB034515 by Capes, Wiley Online Library on [04/11/2026]. See the Terms and Conditions (https://onlinelibrary.wiley.com/terms-and-conditions) on Wiley Online Library for rules of use; OA articles are governed by the applicable Creative Commons License

21699356, 2026, 10, Downloaded from https://agupubs.onlinelibrary.wiley.com/doi/10.1029/2026JB034515 by Capes, Wiley Online Library on [04/11/2026]. See the Terms and Conditions (https://onlinelibrary.wiley.com/terms-and-conditions) on Wiley Online Library for rules of use; OA articles are governed by the applicable Creative Commons License

While these approaches provide important complementary constraints on the shallow volcanic system, they do not directly resolve absolute 3-D body-wave velocity structure at the kilometer and sub-kilometer scales needed to characterize the reservoir system beneath Kīlauea. The ability to resolve fine-scale structure in the uppermost kilometers has been limited by the restricted spatial distribution of permanent seismic stations and the resulting uneven earthquake ray-path coverage. These factors severely limit resolving power in the shallow crust, where magma storage, withdrawal, and deformation are concentrated and where velocity heterogeneity is strongest. Although methodological advances such as waveform cross-correlation relocation and improved parameterization (including finer, adaptive grid spacing and refined damping and regularization schemes) have enhanced imaging fidelity (e.g., Lin & Okubo, 2016; Lin, Shearer, et al., 2014; Matoza et al., 2013), resolution limits imposed by network geometry remain difficult to overcome using existing permanent arrays alone.

Studies at other volcanic systems have demonstrated that dense seismic arrays can substantially improve resolution of shallow magmatic structure. At Mount St. Helens, dense deployments combined with ambient noise tomography enhanced imaging of shallow shear-wave velocity structure associated with magma storage (Y. Wang et al., 2017). At Yellowstone volcano, temporary dense seismic arrays similarly provided improved constraints on shallow magma reservoirs and anisotropic structure through ambient noise analysis (Wu et al., 2023).

Beyond ambient-noise approaches, hybrid experiments that integrate passive earthquakes with controlled active sources have further sharpened images of volcanic plumbing systems. Such experiments, and the purely active-source surveys that preceded them, have a long history at volcanoes worldwide and provide the closest precedents for the present study. Active-source surveys have proven effective at calderas: at Campi Flegrei the SERAPIS survey resolved the buried caldera rim and shallow velocity structure (Zollo et al., 2003), and at Mount Vesuvius the TOMOVES and related experiments imaged a mid-crustal low-velocity zone and an extended magmatic sill (Auger et al., 2001; Zollo et al., 1996). Comparable surveys have constrained shallow structure and conduit geometry at stratovolcanoes, including Merapi volcano in Indonesia, where dense deployments characterized shallow scattering and velocity structure (Wegler & Lühr, 2001), Mount Asama and Mount Iwate in Japan (Aoki et al., 2009; Tanaka et al., 2002), and Mount Erebus in Antarctica (Zandomeneghi et al., 2013). Experiments that invert active and passive arrivals together are closer analogs still: TOMO-ETNA combined active marine shots with local seismicity beneath Mount Etna (Ibáñez et al., 2016), and SEA-CALIPSO at Soufrière Hills volcano, Montserrat, combined onshore-offshore active sources with passive recordings to image the upper crust of an active arc volcano (Paulatto et al., 2010; Shalev et al., 2010). The experiment described below builds on these efforts and is distinguished by its exceptional nodal density, its very large vibroseis data set, and the joint inversion of passive and active-source arrivals on a 500 m parameterization beneath an active summit caldera.

Between 2 May and 8 June of 2023, a large-scale seismic experiment was conducted to re-examine the summit region of Kīlauea using an unprecedentedly dense array. More than 1,800 three-component seismic nodes were deployed across the summit and caldera, recording both passive local earthquakes and active-source signals generated by a triaxial vibroseis buggy (Denlinger et al., 2024). This hybrid experimental design provided complementary ray coverage, with active sources offering well-controlled constraints on shallow structure and earthquakes sampling deeper portions of the volcanic edifice. Together, these data sets enable construction of high-resolution 3-D velocity models beneath the summit caldera that are not achievable with permanent networks alone.

In this study, we apply body-wave tomography to the combined active-source and passive earthquake data sets to invert for V_p, V_s, and V_p/V_s beneath Kīlauea's summit. The resulting models provide new constraints on the geometry, extent, and physical state of shallow magma storage and its connections within the summit region. By leveraging dense nodal observations and a hybrid data strategy, this work builds on earlier seismic imaging studies at Kīlauea and extends them to substantially finer spatial scales. More broadly, the experiment demonstrates the capability of large-N nodal deployments to achieve sub-kilometer to kilometer-scale imaging in complex volcanic environments, offering new perspectives on how magma is stored, connected, and mobilized within the shallow crust and pointing toward a new standard for investigating active magmatic systems worldwide.

21699356, 2026, 10, Downloaded from https://agupubs.onlinelibrary.wiley.com/doi/10.1029/2026JB034515 by Capes, Wiley Online Library on [04/11/2026]. See the Terms and Conditions (https://onlinelibrary.wiley.com/terms-and-conditions) on Wiley Online Library for rules of use; OA articles are governed by the applicable Creative Commons License

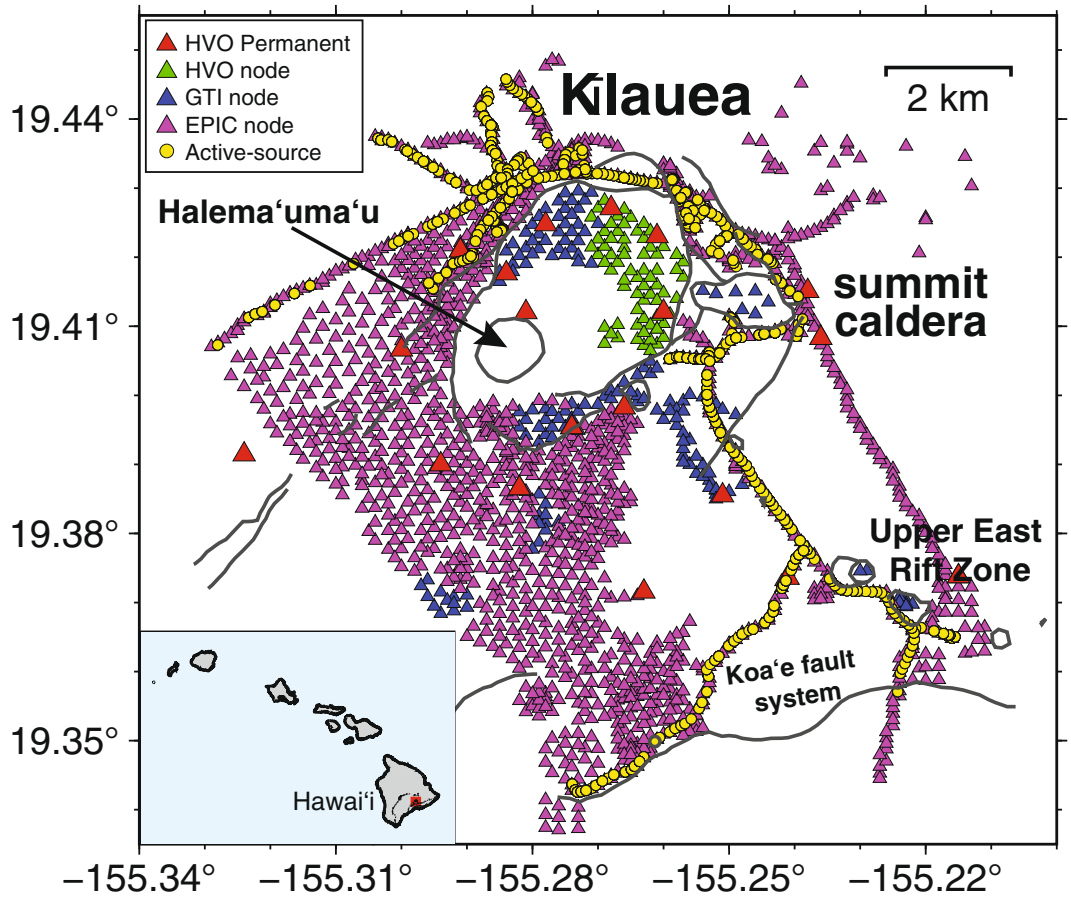


Figure 1. Seismic experiment layout at the summit of Kīlauea during the 2023 deployment. Red triangles indicate permanent seismic stations operated by the Hawaiian Volcano Observatory (HVO). Temporary three-component seismic nodes are shown in green (HVO, 83), blue (Geophysical Technology, Inc. [GTI], 152), and magenta (EarthScope Primary Instrument Center [EPIC], 1,580). Yellow circles mark the 396 T-Rex vibroseis shot locations. Gray lines denote mapped faults, eruptive fissures, and crater and caldera rims of the summit region. Labeled features are the summit caldera, Halema'uma'u crater, the Upper East Rift Zone, and the Koa'e fault system. The inset shows the Hawaiian Islands, with the red box on the Island of Hawai'i marking the experiment area.

2. Experiment and Data Set

2.1. Deployment Overview

Given the heightened volcanic and seismic activity across Hawai'i, particularly following the 2018 Kīlauea eruption, temporary dense seismic arrays have increasingly been deployed at Kīlauea and elsewhere on the Island of Hawai'i to achieve high spatial resolution for imaging volcanic structure and monitoring eruptive processes (Denlinger et al., 2024; Janiszewski et al., 2024; Lanza et al., 2025; Wei et al., 2020; Wu et al., 2020; Yang et al., 2026). The tomographic analysis presented in this study is based on seismograms recorded by an extensive passive- and active-source seismic experiment conducted at the summit of Kīlauea from May to June 2023 (Denlinger et al., 2024). The deployment geometry, station distribution, and active-source layout are shown in Figure 1. A total of 1,815 three-component seismic nodes were deployed across the summit region, covering an area of approximately 12 × 12 km and providing exceptionally dense spatial sampling of the shallow volcanic edifice.

The array incorporated multiple types of three-component nodes, with different sensor natural frequencies to achieve both high spatial density and broad frequency sensitivity, including 1,580 SmartSolo short-period 5 Hz nodes from the EarthScope Primary Instrument Center (EPIC; formerly the IRIS PASSCAL Instrument Center), 152 intermediate-frequency (2 Hz) nodes from Geophysical Technology, Inc. (GTI), and 83 low-frequency

21699356, 2026, 10, Downloaded from https://agupubs.onlinelibrary.wiley.com/doi/10.1029/2026JB034515 by Capes, Wiley Online Library on [04/11/2026]. See the Terms and Conditions (https://onlinelibrary.wiley.com/terms-and-conditions) on Wiley Online Library for rules of use; OA articles are governed by the applicable Creative Commons License

(0.2 Hz) SmartSolo nodes provided by the U.S. Geological Survey (USGS) Hawaiian Volcano Observatory (HVO). Station spacing in the central summit region was typically 100–200 m, enabling sensitivity to sub-kilometer heterogeneity in the upper crust.

Most EPIC nodes were deployed on unconsolidated volcanic substrates using ground spikes to promote good coupling. For about 100 EPIC nodes, substrate conditions such as competent lava flows, paved surfaces, or limited soil cover were less favorable, and those sensors were installed in weighted sand buckets to improve coupling and reduce site effects. The GTI and HVO nodes had triaxial leveling legs and were deployed on hard lava surfaces. Similar installation strategies have been used successfully in temporary dense seismic arrays deployed on volcanic terrains (e.g., Janiszewski et al., 2024; Wu et al., 2020; Yang et al., 2026). Together, these approaches provided dense and relatively uniform coverage across the caldera and surrounding summit region while accommodating logistical and safety constraints.

Controlled-source seismic experiments have proven effective for resolving shallow velocity structure in volcanic and geothermal settings, particularly when implemented with dense receiver arrays (e.g., Aoki et al., 2009; Shalev et al., 2010; Wegler & Lühr, 2001; Zandomeneghi et al., 2013). Building on this approach, the 2023 Kīlauea seismic experiment incorporated active-source data generated by a 30,390 kg triaxial vibroseis truck (T-Rex) operated by the Natural Hazards Engineering Research Infrastructure (NHERI) at the University of Texas at Austin. The T-Rex system generated controlled vertical and horizontal vibrations over a frequency range of 5–28 Hz at 396 source locations distributed along paved roads within the summit region (yellow circles in Figure 1). Seismic energy from these sources was recorded by the full nodal array as well as by permanent stations of the USGS HVO seismic network, providing dense short-offset ray coverage that strongly constrains near-surface velocity variations. Accelerometers installed at each source site monitored ground motion in real time to ensure vibration amplitudes remained below established permitting and safety thresholds.

The controlled and repeatable nature of the vibroseis source, combined with dense station spacing, yields high-quality active-source travel-time data that complement passive earthquake observations and strengthen resolution of the shallow summit structure. Full details of the experimental design, instrumentation, logistics, and safety considerations are provided by Denlinger et al. (2024).

2.2. Earthquake Catalog

Passive-source *P*- and *S*-wave arrival times used in this study were estimated using three automated picking approaches: short-term-average/long-term-average (STA/LTA) (e.g., Allen, 1978; Earle & Shearer, 1994; Jones & van der Baan, 2015), the RESTX package (Comte et al., 2019), which is based on the autoregression algorithms of Pisarenko et al. (1987), and PhaseNet (e.g., Zhu & Beroza, 2019a), a widely used deep-neural-network-based picker. The primary reason for using multiple approaches was to exploit their complementary strengths: RESTX and STA/LTA tend to perform well for *P* arrivals because they are relatively waveform agnostic, whereas PhaseNet often performs better for more complex *S* arrivals because it is trained on labeled seismic waveforms. In practice, the final *P* arrivals were drawn primarily from RESTX and STA/LTA and the final *S* arrivals primarily from PhaseNet. Where picks from different methods overlapped, their agreement served as an automated quality check, and arrivals were retained when the independent estimates were mutually consistent. Phase association and preliminary event locations were carried out within the RESTX framework (Comte et al., 2019). This catalog is therefore referred to throughout as the RESTX catalog.

Application of STA/LTA and RESTX resulted in detection of more than 35,000 potential earthquakes within a 30 km radius of Kīlauea's summit. The STA/LTA and RESTX detections were generated independently and subsequently merged. A preliminary catalog of the larger-magnitude events was first constructed using only the permanent HVO network, because most events of usable size are well recorded there. This HVO catalog, together with the STA/LTA catalog, was then used to guide detection and association across the dense nodal array. Within the RESTX framework, individual station detections were associated into candidate events based on the number of detections falling within a moving time window scaled to the apparent wave speeds across the network, using the one-dimensional (1-D) layer-average model of Lin, Shearer, et al. (2014) to predict *P*- and *S*-wave travel times. Because RESTX was developed for sparser, regional-scale deployments, its default association criteria are poorly suited to the station spacing (∼100 m) and station count (∼1,800) here, which together yield a very low detection threshold and a correspondingly large number of candidate detections. We therefore raised the minimum number of associated detections required to declare an event. This choice reflects the imaging objective of

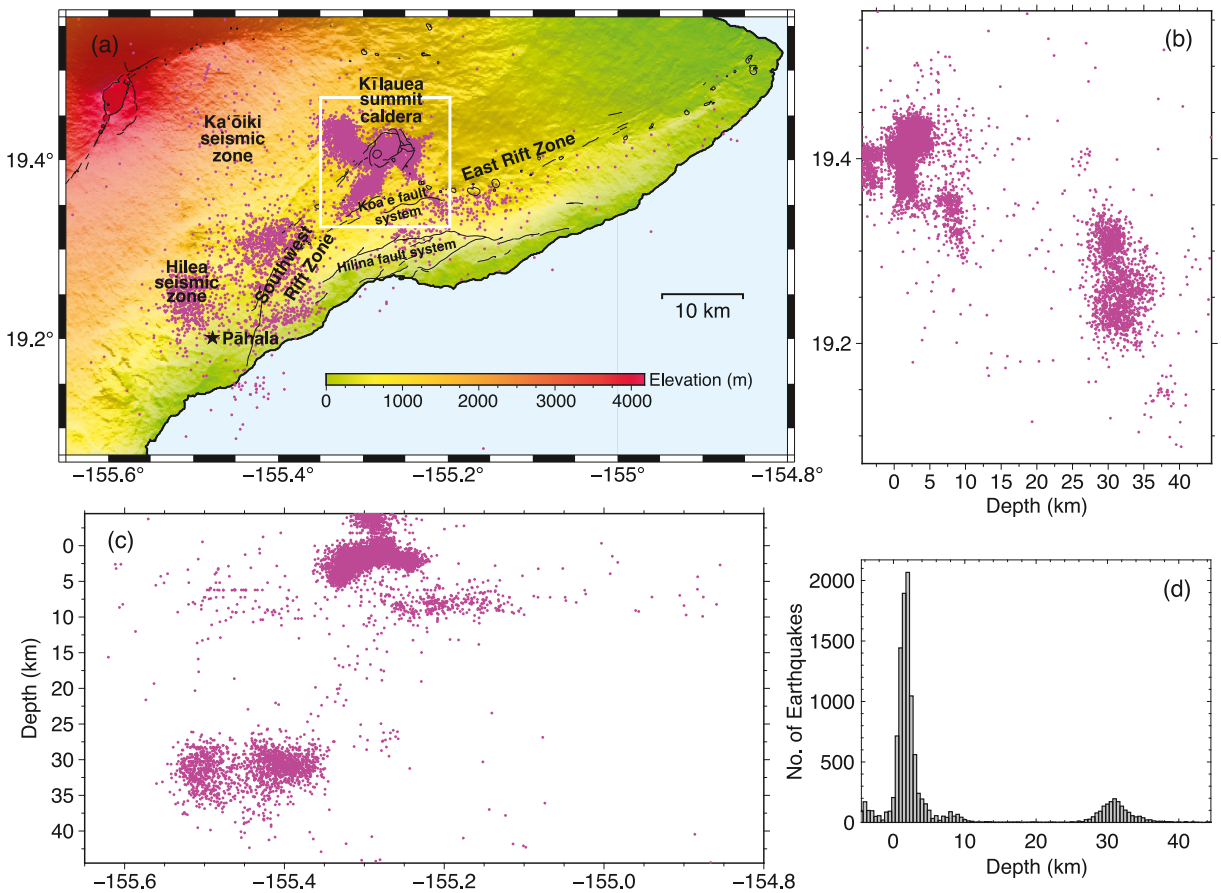


Figure 2. Earthquake distribution recorded during the 2023 experiment. (a) Map view of 12,150 earthquake epicenters (magenta dots) across the southeastern Island of Hawai'i, underlain by shaded topography (color scale). Black lines denote mapped faults, rift zones, and eruptive fissures, together with crater and caldera rims and the coastline. Labeled features are the Kīlauea summit caldera, the Koa'e and Hilina fault systems, the Southwest and East Rift Zones, and the Ka'ōiki and Hilea seismic zones. The black star marks Pāhala. The white box outlines the summit inversion region beneath Kīlauea. (b) Earthquake latitude versus depth and (c) longitude versus depth. (d) Histogram of earthquake depths, highlighting shallow seismicity beneath the summit (<10 km) and a deeper cluster beneath the Pāhala region (∼30 km).

this study, emphasizing events recorded across many tens of stations that are most useful for tomography, rather than seeking catalog completeness for the smallest events. For 12,150 of the best-recorded events, onset estimates from the three algorithms were combined to generate an initial catalog containing about 10 million *P* arrivals and 5 million *S* arrivals (Figures 2a–2c, Roecker et al., 2026). Initial *P*- and *S*-wave arrival times were spot-checked manually to ensure consistency and accuracy across the dense nodal array. Manual review was concentrated in the early stages of processing, when close to 100% of the picks were inspected in order to verify the behavior of the automated algorithms and to tune their control parameters. Once the pickers performed as expected, review was targeted at events that retained unusual outliers, roughly 10% of the picks, to diagnose the conditions under which the algorithms fail rather than to re-inspect picks that were already well behaved.

The spatial distribution of earthquakes in the RESTX catalog closely follows long-recognized seismicity patterns beneath Kīlauea. The majority of events (9,782 earthquakes) are concentrated beneath the summit region at depths shallower than 10 km, within the summit inversion region (white box in Figure 2a). In contrast, deeper earthquakes extending to depths of approximately 30 km are primarily clustered in the Pāhala region (Figure 2d), consistent with earlier studies documenting deep seismicity beneath the south flank of Hawai'i (e.g., Janiszewski et al., 2024; Klein, 1981; Wolfe et al., 2004). The relationship between *P*- and *S*-wave travel times for the RESTX catalog (Figure S1a in Supporting Information S1), commonly referred to as a Wadati diagram (Wadati & Oki, 1933), provides an empirical basis for selecting an appropriate initial V_p/V_s ratio of 1.74 for the tomographic inversion.

21699356, 2026, 10, Downloaded from https://agupubs.onlinelibrary.wiley.com/doi/10.1029/2026JB034515 by Capes, Wiley Online Library on [04/11/2026]. See the Terms and Conditions (https://onlinelibrary.wiley.com/terms-and-conditions) on Wiley Online Library for rules of use; OA articles are governed by the applicable Creative Commons License

21699356, 2026, 10, Downloaded from https://agupubs.onlinelibrary.wiley.com/doi/10.1029/2026JB034515 by Capes, Wiley Online Library on [04/11/2026]. See the Terms and Conditions (https://onlinelibrary.wiley.com/terms-and-conditions) on Wiley Online Library for rules of use; OA articles are governed by the applicable Creative Commons License

3. Tomographic Inversion

3.1. Tomographic Event Selection

To achieve spatially uniform sampling of the summit region while maintaining computational efficiency, we selected a subset of representative earthquakes as tomographic events for the arrival time inversion. Event selection was guided by local seismicity density and the number of high-quality phase picks available for each event, an approach commonly adopted in local-earthquake tomography to balance spatial coverage and data quality (e.g., Haslinger et al., 2001; Lin, Shearer, et al., 2014; Lin et al., 2007; Thurber et al., 1997). Within each 0.5 km horizontal interval, the earthquake with the largest number of reliable phase arrivals was retained for tomography, ensuring that well-constrained sources dominate the inversion while avoiding excessive clustering of nearby events.

This procedure yielded a total of 799 hypocenters located within the summit inversion region (Figure 3a). Their depth distribution (Figure 3b) is strongly skewed toward shallow depths, peaking at 1–2 km below sea level, with the majority of events shallower than 5 km and only a small number of deeper events, and mirrors the seismicity recorded within the summit inversion region targeted by the tomography (white box in Figure 2a). The resulting passive data set comprises 932,740 *P*-wave and 413,264 *S*-wave first arrivals, corresponding to averages of 1,167 *P* arrivals and 517 *S* arrivals per event. The large number of picks per event reflects both the exceptional station density of the nodal array and the high signal-to-noise ratio of many local earthquakes. The relationship between *P*- and *S*-wave travel times for the selected tomographic events (Figure S1b in Supporting Information S1), estimated using the robust mean method of Lin and Shearer (2007), closely matches that of the full catalog, indicating that the tomographic event subset preserves the statistical and kinematic characteristics of the broader data set. The RESTX catalog is deliberately inclusive: each arrival carries an uncertainty estimate derived from the shape of the picking estimation function, and marginal readings are flagged rather than discarded. Arrivals are flagged when their preliminary residuals relative to the 1-D initial model exceed 1 s or 5% of the travel time, and also when the picking algorithm grades them as problematic on other quality criteria despite acceptable residuals. Prior to inversion we removed all flagged arrivals along with picks that lacked agreement among the independent picking methods. The nodal array provides far more high-quality picks than the inversion requires, so this conservative selection still leaves a large and well-distributed data set.

In addition to the passive earthquake data, the inversion incorporates 209,824 *P*-wave arrivals from 396 active T-Rex vibroseis shots (white dots in Figure 3a), with an average of approximately 530 arrivals per shot. Arrivals from the vibroseis shots were picked within the RESTX framework operating in its source-augmentation mode, in which the known shot locations and origin times (specified through a source table) are used to predict and refine the phase arrivals rather than solving for source parameters, in contrast to the standard detection-and-association mode used for the earthquakes. Although the triaxial T-Rex source radiates both compressional and shear energy, and clear *P* arrivals are observed at many stations from both vertical and horizontal source orientations, we were unable to identify consistent, coherent *S* arrivals on the vibroseis records. We searched for shear arrivals on the appropriate components, including the strong *SV* motion expected on the vertical components at the short source-receiver offsets sampled here, but no coherent shear phase or associated Rayleigh-wave signature could be reliably distinguished from the later wavetrain. The most likely explanation is a near-surface propagation effect: energy injected at the surface into a shallow, strongly scattering, low-V_s waveguide generates intense scattered coda that obscures coherent phases arriving after the direct *P* wave. This interpretation is consistent with the observation that usable *S* arrivals are still recovered from local earthquakes, whose ray paths originate beneath this shallow scattering layer and traverse it only along a short final segment. Isolating the responsible mechanism will require dedicated analysis of the vibroseis wavefield. Regardless of the mechanism, the practical consequence is that the active-source inversion uses *P* arrivals only. The vibroseis sources provide dense, short-offset ray paths that complement the longer-offset earthquake rays and significantly enhance resolution of the shallow subsurface. The combined use of tomographic earthquakes and controlled sources follows established practice in hybrid tomographic studies and has been shown to improve stability and resolution, particularly in the upper crust (e.g., Lin et al., 2010).

3.2. Grid Selection

In travel-time tomography, achievable lateral resolution is fundamentally constrained by the width of the first Fresnel zone, which depends on the dominant seismic wavelength and source-receiver geometry (e.g., Dahlen

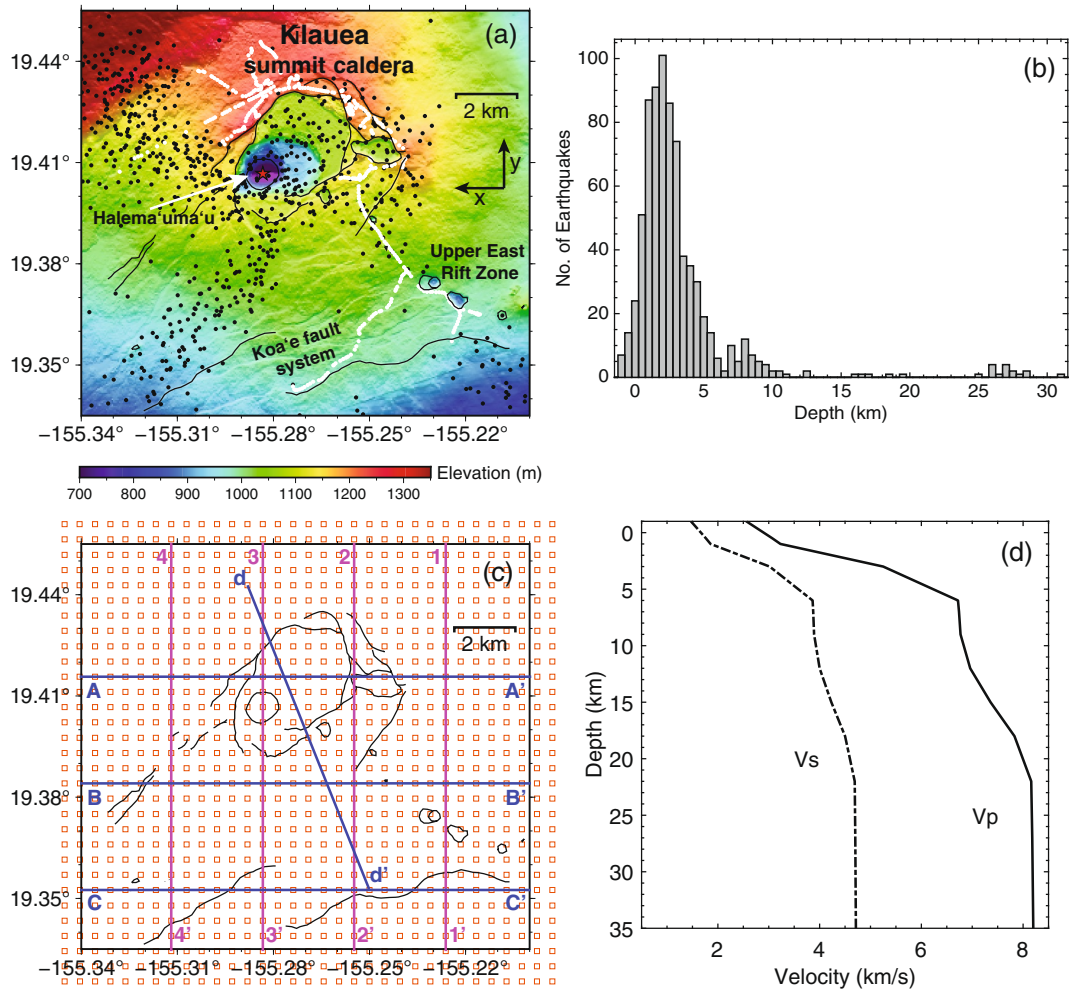


Figure 3. Tomographic events, event-depth histogram, inversion geometry, and one-dimensional (1-D) initial velocity model beneath Kīlauea, Hawai'i. (a) Map view showing surface topography together with 799 tomographic earthquakes (black dots) and 396 T-Rex vibroseis sources (white dots) used in the inversion. The red star marks the Cartesian coordinate origin, with x positive to the west and y positive to the north. (b) Histogram of the depth distribution of the tomographic events used in the inversion, showing that most events are shallower than 5 km beneath the summit, with a small number of deeper events. (c) Map view of the inversion setup. Orange squares indicate the horizontal inversion grid. North–south profiles (1-1′ to 4-4′) are shown as pink lines, and the west–east profiles A-A′, B-B′, and C-C′ together with the northwest–southeast profile d-d' as dark blue lines. These profiles define the locations of the depth views shown in the following figures. (d) 1-D initial V_p model adapted from Lin, Shearer, et al. (2014), together with the corresponding V_s model defined using a constant V_p/V_s ratio of 1.74. Depth is referenced to mean sea level. Here V_p is compressional-wave velocity, V_s is shear-wave velocity, and V_p/V_s is the ratio of the two.

et al., 2000; Nolet, 2008). Following Nolet (2008), we estimate the first-Fresnel-zone diameter as $d \approx \sqrt{\lambda L}$, where $\lambda = v/f$ is the dominant wavelength, f is the dominant frequency, and L is the source-receiver offset. The velocity v is taken from the P- and S-wave profiles of the 1-D initial model (Figure 3d), so the diameters reported below depend jointly on velocity, frequency, and offset and describe a range of finite-frequency sensitivities rather than a single resolution length. For the active-source data set used here, source-receiver offsets ranging from approximately 50 m to 10 km and dominant frequencies of 5–28 Hz yield Fresnel-zone diameters of roughly 70–250 m at near offsets and 1–2.4 km at the largest offsets, evaluated at the shallow P-wave velocity of the 1-D initial model. The near-offset values imply sub-kilometer sensitivity to velocity structure in the shallowest few hundred meters, whereas the larger offsets that sample greater depths carry kilometer-scale sensitivity. Passive earthquake data, recorded predominantly near 5 Hz with offsets extending to 10 km, produce Fresnel diameters of approximately 0.6–3 km for P waves and 0.5–2.3 km for S waves, indicating kilometer-scale resolving power at

21699356, 2026, 10, Downloaded from https://agupubs.onlinelibrary.wiley.com/doi/10.1029/2026JB034515 by Capes, Wiley Online Library on [04/11/2026]. See the Terms and Conditions (https://onlinelibrary.wiley.com/terms-and-conditions) on Wiley Online Library for rules of use; OA articles are governed by the applicable Creative Commons License

21699356, 2026, 10, Downloaded from https://agupubs.onlinelibrary.wiley.com/doi/10.1029/2026JB034515 by Capes, Wiley Online Library on [04/11/2026]. See the Terms and Conditions (https://onlinelibrary.wiley.com/terms-and-conditions) on Wiley Online Library for rules of use; OA articles are governed by the applicable Creative Commons License

greater depth. Representative Fresnel-zone diameters across the dominant frequency and offset ranges are tabulated in Table S1 in Supporting Information S1.

In practice, resolution is further enhanced by the exceptionally dense station spacing, favorable azimuthal coverage, and extensive overlap of ray paths provided by the combined data set, as demonstrated by checkerboard resolution tests. Such coverage improves model stability, reduces trade-offs, and aids recovery of coherent anomalies, but it cannot overcome the finite-frequency sensitivity of the wavefield. Effective resolution is set jointly by Fresnel-zone width, ray-path density and azimuthal coverage, damping, and data noise, so dense sampling brings the model closer to the best resolution these factors permit rather than beyond it (e.g., Rawlinson et al., 2010). Based on these considerations, we adopted a horizontal grid spacing of 500 m for the final velocity models (Figure 3c). This choice is consistent with the minimum resolvable scale supported by the data, minimizes discretization bias, and avoids oversampling that could introduce instability or spurious structure (e.g., Nolet, 2008; Rawlinson et al., 2010). We emphasize that this 500 m value denotes the model parameterization (grid spacing) and not the spatial resolution, which varies across the model and is assessed independently through the ray coverage and resolution tests. The spacing was chosen to be fine enough to represent the data-supported structure implied by the Fresnel-zone estimates above, yet coarse enough to avoid over-parameterization and spurious small-scale features. The final model was selected after inversions using various horizontal grid spacings and rotated inversion grids, across which the principal velocity anomalies are robust within the well-resolved areas. Finer parameterizations proved computationally prohibitive for the full data set, so we adopt 500 m as the finest discretization it can support in practice.

Vertical discretization employs variable layer spacing. All depths in this paper are referenced to mean sea level (MSL), unless otherwise noted. From 1.5 km above to 1 km depth, layers are defined at 0.5 km intervals to capture fine-scale shallow structure where velocity gradients are strongest. From 2 to 7 km depth, layer spacing is increased to 1 km, while below 7 km depth, progressively coarser spacing ranging from 2 to 8 km is used to stabilize the inversion and reflect the decreasing resolving power at depth. Such variable vertical parameterization is commonly employed in volcanic tomography to balance resolution and stability across a wide depth range (e.g., Haslinger et al., 2001; Lin, Shearer, et al., 2014; Thurber, 1993). The inversion grid has a flat top referenced to MSL, and topography is incorporated through the station and shot elevations used in ray tracing rather than through a deformed top surface. The grid is extended to 35 km only to provide a stable far-field boundary for ray tracing. The experiment provides essentially no turning rays at those depths, so nodes below about 5 km remain at or very near their 1-D initial values, and no structure is interpreted below 4 km depth.

3.3. Initial Model

The initial velocity model for the tomographic inversion was constructed from a layer-averaged V_p profile extracted from the regional 3-D model of Lin, Shearer, et al. (2014), which provides a geologically and geophysically consistent representation of the average crustal velocity structure beneath Hawai'i and serves as an appropriate background for local-scale inversion. A corresponding V_s profile was derived by assuming a constant V_p/V_s ratio of 1.74, consistent with the robust mean slope of observed *P*- and *S*-wave travel-time pairs from the earthquake catalog (Figure S1 in Supporting Information S1). Similar constant-ratio initial models are widely used in joint V_p and V_p/V_s inversions and provide a stable reference for resolving 3-D velocity perturbations (e.g., Eberhart-Phillips, 1990; Thurber, 1993). This 1-D model represents the average velocity structure beneath the summit region of Kīlauea and was used as the starting point for all inversions (Figure 3d). Although the choice of initial model can influence convergence, previous studies have shown that sufficiently dense data coverage, such as that available here, reduces sensitivity to reasonable variations in the initial model (e.g., Haslinger et al., 2001; Lin, Shearer, et al., 2014; Rawlinson et al., 2010). We nonetheless acknowledge that, because the inverse problem is nonlinear, the absolute velocities, anomaly amplitudes, and detailed anomaly geometry may retain some dependence on the 1-D initial model, particularly for long-wavelength lateral structure that a 1-D profile cannot represent. We therefore emphasize relative velocity perturbations and the locations of well-resolved anomalies rather than absolute values, especially in less well-resolved regions. The final model was likewise selected after testing alternative 1-D initial models, and the recovered anomalies within the well-resolved regions are insensitive to these choices.

21699356, 2026, 10, Downloaded from https://agupubs.onlinelibrary.wiley.com/doi/10.1029/2026JB034515 by Capes, Wiley Online Library on [04/11/2026]. See the Terms and Conditions (https://onlinelibrary.wiley.com/terms-and-conditions) on Wiley Online Library for rules of use; OA articles are governed by the applicable Creative Commons License

3.4. Inversion Approach

Tomographic inversions were performed using the SIMUL2000 algorithm (Eberhart-Phillips, 1990; Thurber, 1983, 1993). SIMUL2000 is a full-matrix, damped least squares inversion framework originally developed for local-earthquake tomography and later extended to accommodate controlled-source data. The algorithm jointly inverts *P*-wave arrival times and *S* - *P* times to solve for earthquake hypocenter parameters, V_p, and V_p/V_s variations.

Model updates are obtained iteratively using parameter-separation techniques (Pavlis & Booker, 1980; Spencer & Gubbins, 1980), in which hypocentral adjustments are estimated separately and velocity updates are then derived from the remaining residual signal, together with damping to stabilize the inversion. At each iteration the earthquake hypocenters are relocated in the current 3-D velocity model, the velocity parameters are updated from the post-relocation residuals, and the cycle is repeated until the travel-time residuals stabilize. We use the term "joint" in this sense, to denote the simultaneous solution for hypocentral and velocity parameters via parameter separation, rather than a single fully coupled linear inversion. This formulation has been widely applied in volcanic and tectonic settings and is well suited to dense local data sets with strong lateral heterogeneity (e.g., Eberhart-Phillips & Michael, 2004; Haslinger et al., 2001; Lin & Thurber, 2012). As part of the inversion, resolution and model covariance matrices are computed, providing quantitative measures of spatial resolution and parameter uncertainty that inform interpretation of the final models. Arrival times were weighted according to their estimated reading quality, with the same quality-based weighting applied to the *P* and *S* - *P* data. Active-source arrivals were assigned twice the weight of passive-earthquake arrivals in the inversion. The inversion incorporates more than 0.9 million *P* and 0.4 million *S* arrivals from the tomographic events in addition to the active-source data. Each iteration therefore requires ray tracing for every source-receiver pair, followed by assembly and solution of a large sparse sensitivity matrix, which makes each full inversion computationally expensive.

3.5. Damping Parameter Selection

Selection of appropriate damping parameters is a critical step in balancing data fit against model smoothness and suppressing unphysical complexity in tomographic inversions (e.g., Eberhart-Phillips, 1986; Thurber, 1993). Damping tests were conducted sequentially. First, the V_p/V_s model was held fixed while a range of damping values for V_p was explored to identify an optimal trade-off between misfit reduction and model roughness. The optimal value was chosen near the point of maximum curvature of the trade-off curve. That is, we selected the smallest damping that does not produce a significant increase in data misfit (Figure S2 in Supporting Information S1). Once the optimal V_p damping was determined, that value was fixed and damping for the V_p/V_s model was selected using the same maximum-curvature criterion.

Trade-off curves illustrating these tests are shown in Figure S2 in Supporting Information S1. The final inversion adopts damping values of 300 for V_p and 100 for V_p/V_s. Similar damping strategies have been shown to yield stable and interpretable results in other local-earthquake tomography studies (e.g., Eberhart-Phillips et al., 1995; Lin, Shearer, et al., 2014). Together, these damping choices provide a robust basis for interpreting both the V_p and V_p/V_s models derived from the combined active and passive data sets.

4. Resolution Assessment

To evaluate the spatial resolving power of the tomographic inversion and to guide interpretation of the final velocity models, we performed a suite of synthetic resolution tests. Checkerboard tests remain a standard and informative diagnostic for local-earthquake tomography, as they provide a direct assessment of how well the data geometry, inversion parameterization, and regularization recover known structure (e.g., Haslinger et al., 2001; Rawlinson et al., 2010; Thurber, 1993). In all tests, synthetic travel times were computed using the same station-event geometry, ray tracing, grid parameterization, and damping as the real data set, and were inverted from the same 1-D initial model through the same iterative procedure, with earthquake hypocenters relocated at each iteration as in the inversion of the observed data. The tests therefore measure the resolving power of the full procedure rather than of the velocity step alone.

The synthetic true models consist of 3-D checkerboard perturbations with 1 km horizontal spacing, corresponding to two inversion grid intervals, and alternating sign between adjacent depth layers to evaluate potential vertical

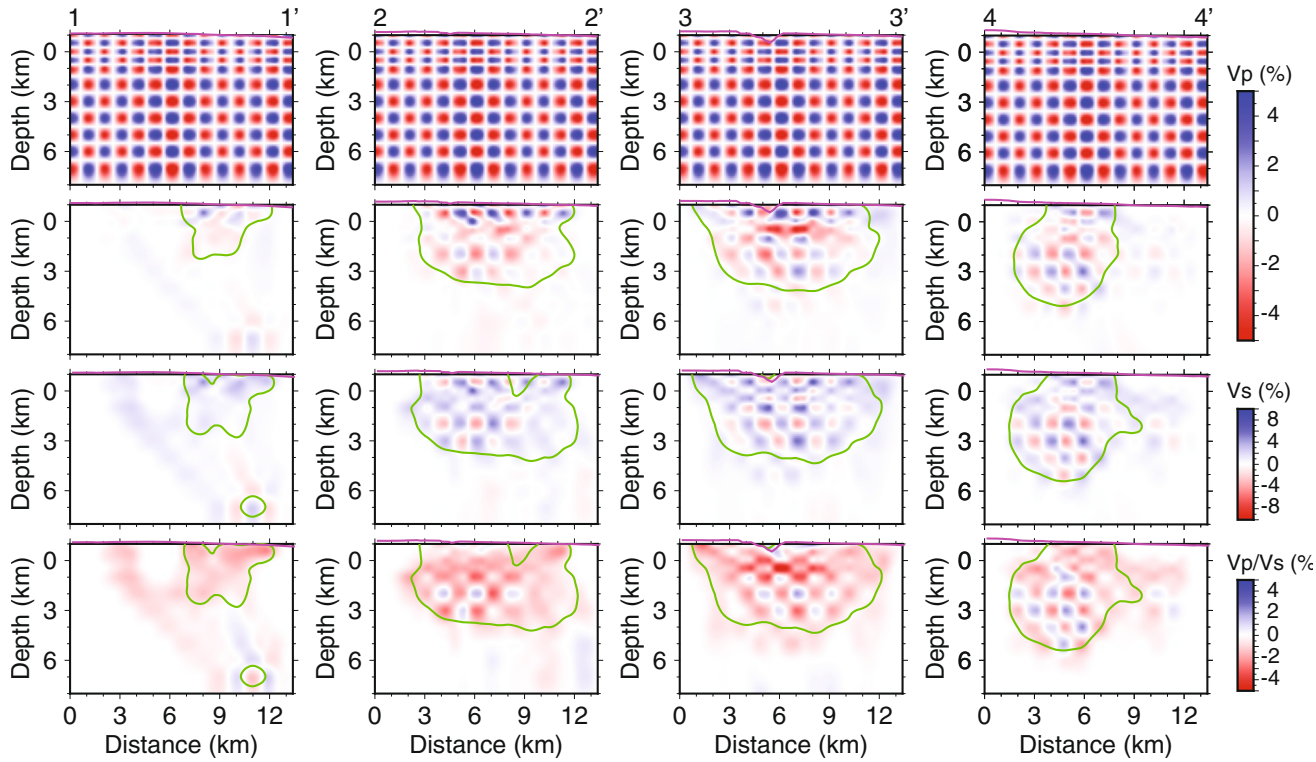


Figure 4. Depth cross-sections from the checkerboard resolution test along the north–south profiles (1-1′ to 4-4′, shown as pink lines in Figure 3c), using the combined active-source and passive data sets. Each column is one profile, labeled above the panels. From top to bottom, the rows show the true V_p checkerboard model and the recovered V_p, V_s, and V_p/V_s models, each plotted as a percentage perturbation. The imposed perturbations are ±5% on V_p and ∓5% on V_p/V_s, so the V_p/V_s rows are of opposite polarity to the V_p rows, and the implied V_s perturbation is ±10%. The three color scales at the right apply to the true and recovered V_p rows, the V_s row, and the V_p/V_s row. Green contours mark the 0.3 resolution threshold, and a magenta line at the top of each section indicates surface topography. Checkerboard cells are 1 km in the horizontal, two inversion grid intervals, and the sign reverses between adjacent depth layers. Depths are relative to mean sea level. Here V_p is compressional-wave velocity, V_s is shear-wave velocity, and V_p/V_s is the ratio of the two.

smearing. Perturbations are imposed on the two models actually inverted for, +5% on V_p paired with −5% on V_p/V_s in the same cell (and vice versa), giving exactly anticorrelated perturbation patterns and an implied V_s perturbation of approximately ±10%. These amplitudes were chosen to be representative of the magnitude of velocity variations commonly inferred beneath active volcanic systems (e.g., Dawson et al., 1999; Lin, Shearer, et al., 2014). Recovered models were compared directly with the true patterns to assess spatial fidelity, amplitude recovery, and the effects of damping and data coverage. With the adopted damping, the 1 km checkerboard is recovered across much of the summit region without noticeable artifacts or excessive smoothing, and adjacent cells remain distinct rather than merging, so the effective resolution in the best-sampled part of the summit is somewhat finer than the 1 km cell size. Together with the restoration and spike tests described below, the checkerboard defines the scales at which the models can be interpreted.

4.1. Resolution of V_p, V_s, and V_p/V_s

The checkerboard tests establish where each model can be interpreted: V_p is resolved over a larger volume than V_s and V_p/V_s, the difference is concentrated above sea level, and over the 1–4 km depth interval that contains the interpreted reservoirs the three models are resolved comparably. Checkerboard results for the combined data set are shown as depth cross-sections in Figures 4 and 5, and as map-view slices for V_p, V_s, and V_p/V_s in Figures S3–S5 in Supporting Information S1. V_p is resolved over a larger volume than V_s and V_p/V_s, and the difference is concentrated above sea level: the *S*-derived models have no resolved region at −1.5 km depth and a smaller one between −1 and 0 km, whereas between 1 and 3 km depth the resolved volumes are comparable. Above sea level, recovered amplitudes within the commonly resolved volume are also lower for V_s and lowest for V_p/V_s. Between 1 and 4 km depth the recovered amplitudes of the three models are similar. This pattern reflects two fundamental

21699356, 2026, 10, Downloaded from https://agupubs.onlinelibrary.wiley.com/doi/10.1029/2026JB034515 by Capes, Wiley Online Library on [04/11/2026]. See the Terms and Conditions (https://onlinelibrary.wiley.com/terms-and-conditions) on Wiley Online Library for rules of use; OA articles are governed by the applicable Creative Commons License

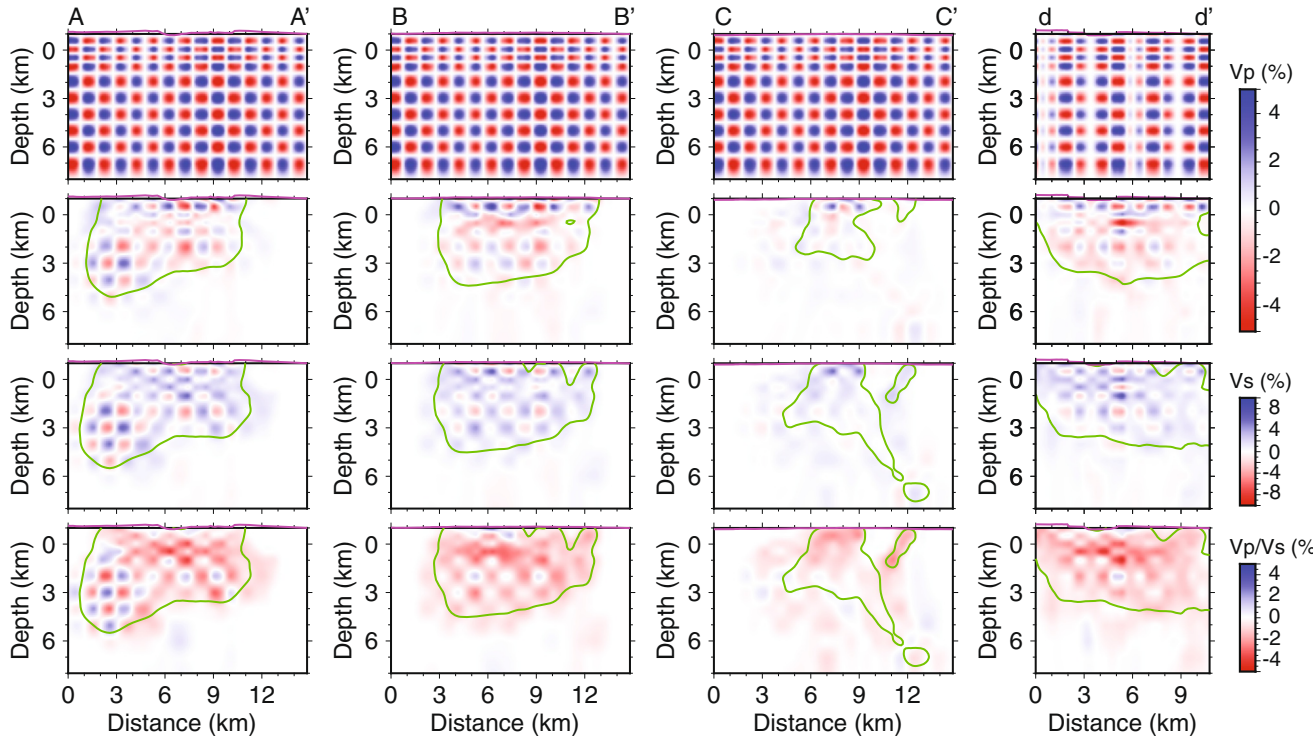


Figure 5. Depth cross-sections from the checkerboard resolution test along the west–east and oblique profiles (A-A′, B-B′, C-C′, and d-d′, shown in Figure 3c), using the combined active-source and passive data sets. Each column is one profile, labeled above the panels. From top to bottom, the rows show the true V_p checkerboard model and the recovered V_p, V_s, and V_p/V_s models, each plotted as a percentage perturbation. The imposed perturbations are ±5% on V_p and ∓5% on V_p/V_s, so the V_p/V_s rows are of opposite polarity to the V_p rows, and the implied V_s perturbation is ±10%. The three color scales at the right apply to the true and recovered V_p rows, the V_s row, and the V_p/V_s row. Green contours mark the 0.3 resolution threshold, and a magenta line at the top of each section indicates surface topography. Checkerboard cells are 1 km in the horizontal, two inversion grid intervals, and the sign reverses between adjacent depth layers. Depths are relative to mean sea level. Here V_p is compressional-wave velocity, V_s is shear-wave velocity, and V_p/V_s is the ratio of the two.

aspects of the data set: the absence of *S*-wave arrivals from the active-source vibroseis data and the smaller number and less uniform distribution of high-quality *S*-wave arrivals in the passive earthquake catalog. Similar resolution differences among V_p, V_s, and V_p/V_s are well documented in local-earthquake tomography studies that rely on joint inversion of *P*-wave travel times and *S* - *P* times (e.g., Eberhart-Phillips, 1990; Haslinger et al., 2001; Lin, Shearer, et al., 2014).

Checkerboard tests for V_p (Figure S3 in Supporting Information S1) show robust recovery from approximately −1 to 4 km depth beneath much of the summit region, with the strongest resolution between −1 and −0.5 km depth. Within this depth range, checkerboard features are laterally continuous and exhibit limited vertical smearing, indicating that the adopted grid spacing and damping parameters are well matched to the resolving power of the data. Recovery does not, however, degrade monotonically with depth. All three models pass through a marked minimum between 0 and 0.5 km depth, the interval over which the dominant constraint shifts from the active-source arrivals to the earthquake rays, and improve again below it. The shallowest slice, at −1.5 km, lies above the summit topography over essentially the whole map and is not recovered. Resolution weakens below about 4 km depth, particularly outside the caldera, reflecting reduced ray density at depth.

Resolution of V_s is more limited and spatially variable (Figure S4 in Supporting Information S1). Meaningful recovery is achieved primarily between approximately −1 and 4 km depth beneath the summit. Recovery is most laterally continuous between 1 and 3 km depth, where the resolved region is largest. At −1.5 km depth no region is resolved at all, owing to the lack of usable *S*-wave constraints. Between 0 and 0.5 km depth V_s passes through the same marked minimum as the other two models, and we interpret shallow V_s structure with corresponding caution.

21699356, 2026, 10, Downloaded from https://agupubs.onlinelibrary.wiley.com/doi/10.1029/2026JB034515 by Capes, Wiley Online Library on [04/11/2026]. See the Terms and Conditions (https://onlinelibrary.wiley.com/terms-and-conditions) on Wiley Online Library for rules of use; OA articles are governed by the applicable Creative Commons License

21699356, 2026, 10, Downloaded from https://agupubs.onlinelibrary.wiley.com/doi/10.1029/2026JB034515 by Capes, Wiley Online Library on [04/11/2026]. See the Terms and Conditions (https://onlinelibrary.wiley.com/terms-and-conditions) on Wiley Online Library for rules of use; OA articles are governed by the applicable Creative Commons License

The V_p/V_s model is resolved primarily between approximately 1 and 4 km depth, best between 2 and 3 km, together with a separate shallow patch between −1 and −0.5 km (Figure S5 in Supporting Information S1). Between 0 and 0.5 km depth the checkerboard is not recovered, and we do not interpret V_p/V_s structure in that interval. Recovered amplitudes are weakest south and east of the caldera where *S*-wave ray coverage decreases. These amplitude trade-offs between V_s and V_p/V_s reflect inherent limitations of joint inversion and underscore the importance of interpreting velocity ratios in conjunction with absolute velocities and resolution metrics (e.g., Eberhart-Phillips, 1990). Because V_p/V_s is inverted directly from the $S-P$ times rather than formed by dividing independently inverted V_p and V_s, its reliability depends on adequate $S-P$ ray coverage, and we interpret it with caution where that sampling is sparse.

Throughout this study, the interpreted volume is delimited by the 0.3 contour of the diagonal elements of the resolution matrix. This threshold is specific to our parameterization. For a fixed data set, a finer grid distributes the same ray coverage over more model parameters, so the diagonal values obtained on the 500 m grid used here are systematically smaller than those of a coarser or more sparsely parameterized model, and a threshold carried over from such a study would not mean the same thing. We therefore selected the level empirically, from the recovery achieved across the synthetic tests presented here and in Supporting Information S1, and from the derivative-weight-sum (ray density) distributions, shown as map-view slices for V_p, V_s, and V_p/V_s in Figures S6 and S7 in Supporting Information S1. The principal interpreted anomalies beneath Halema'uma'u and the south caldera lie well inside this boundary, so the main features do not depend on the precise choice of level.

4.2. Dataset-Specific V_p Resolution Tests

To demonstrate the contributions of the different data types and the advantage of combining active- and passive-source observations, we performed three additional checkerboard tests that invert exclusively for V_p: one using active-source data alone, one using tomographic earthquake data alone, and one using the combined data set. These tests follow established practice in hybrid tomography studies and provide a direct illustration of the complementary resolving power of controlled sources and natural earthquakes.

The active-source-only test (Figures S8 and S9 in Supporting Information S1) demonstrates excellent near-surface resolution from approximately −1 to 0.5 km depth beneath the summit, reflecting dense short-offset ray coverage from the vibroseis shots. Resolution degrades rapidly below approximately 1 km depth, consistent with the limited penetration of vibroseis energy and the absence of longer-offset ray paths.

In contrast, the tomographic-earthquake-only test (Figures S10 and S11 in Supporting Information S1) provides limited shallow resolution but yields improved recovery below approximately 0.5 km depth and its strongest recovery between 1 and 4 km, with resolvable structure extending locally to greater depths. This pattern reflects the longer ray paths and broader azimuthal coverage provided by natural earthquakes, which are essential for constraining deeper velocity structure beneath the summit.

The combined V_p-only data set test (Figures S12 and S13 in Supporting Information S1) integrates the complementary strengths of the two data types, with active-source observations stabilizing shallow structure and tomographic earthquake rays constraining deeper regions. The resulting V_p recovery is the most laterally continuous and vertically extensive of the three dataset-specific tests. Because it solves for V_p alone, it also confirms that the resolved V_p structure is not an artifact of the joint inversion for V_p and V_p/V_s.

4.3. Restoration and Spike Tests

In order to complement the checkerboard, whose perturbations are aligned with the inversion grid, we performed a restoration test, which inverts noisy synthetic travel times computed through the final 3-D model itself, and a spike test, which places isolated compact bodies at the two interpreted targets (Figures S14 and S15 in Supporting Information S1). The restoration test recovers the major interpreted features in place from noisy data, though systematically weaker than the true model. The spike test uses idealized bodies at the same two locations rather than the imaged anomalies themselves, so it measures the point-spread response there rather than validating the anomaly shapes: an isolated body is recovered essentially in place and without measurable broadening, but with a peak amplitude that can exceed the true one. The spike test also shows that a compact low-velocity body at 0.5–2 km depth generates on its own an apparent V_p/V_s high about 1.5 km above and 2 km laterally offset from

21699356, 2026, 10, Downloaded from https://agupubs.onlinelibrary.wiley.com/doi/10.1029/2026JB034515 by Capes, Wiley Online Library on [04/11/2026]. See the Terms and Conditions (https://onlinelibrary.wiley.com/terms-and-conditions) on Wiley Online Library for rules of use; OA articles are governed by the applicable Creative Commons License

itself, so shallow high-V_p/V_s features offset above a resolved low-velocity body are not independently constrained.

4.4. Limitations of the Resolution Tests

All three tests share the premises of the inversion itself, using the same acquisition geometry, ray-theoretical forward calculation, isotropic parameterization, and damping. They therefore measure how well that procedure recovers structure it can represent, not error introduced by the assumptions themselves. Each is also limited by the structure it assumes. The checkerboard is aligned with the inversion grid and spans only two grid intervals, so it probes structure near the finest data-supported scale and is least informative for compact, inclined, or strongly 3-D anomalies. Longer-wavelength anomalies are recovered more robustly. The restoration test uses the imaged model as its own true model, and the spike test uses assumed shapes at the interpreted locations. None can reveal structure the data failed to image. Because recovered amplitudes also depend on the adopted damping, and useful resolution contracts sharply below 3 km, all three establish the existence and approximate location of anomalies far more firmly than their shape, extent, and amplitude. We therefore interpret no structure below 4 km, and treat anomaly geometries as features permitted by the data and the adopted parameterization rather than as uniquely resolved structures.

5. Final Seismic Velocity Models

5.1. *P*-Wave Velocity Model

The final V_p model exhibits complex 3-D structure beneath the summit region of Kīlauea, with well-resolved velocity variations from approximately −1 to 4 km depth (Figure 6). These results reflect contributions from both active-source and tomographic-earthquake ray paths and are constrained within the 0.3 resolution threshold defined from synthetic tests. Checkerboard recovery (Figure S3 in Supporting Information S1) is strongest between −1 and −0.5 km and again between 1 and 3 km depth, with a marked minimum at 0–0.5 km. In the western part of the model domain resolution extends to approximately 4 km depth, supported by steeper earthquake ray paths beneath the summit. Together, these observations provide a high-resolution image of the upper crust beneath the summit caldera within the best-resolved part of the model.

The −1.5 km slice (Figure 6a) lies above the summit topography almost everywhere and is not recovered by the checkerboard test. It is shown for completeness only and is not interpreted. At −1 km relative to MSL (Figure 6b), low-velocity anomalies encircle the summit caldera, whereas the caldera interior exhibits relatively high velocities. These peripheral low-V_p zones form a ring-like pattern that broadly follows the caldera boundary. At −0.5 km depth (Figure 6c), the velocity pattern changes markedly, with high velocities dominating much of the resolved area, particularly along the north and northeast rim of the caldera. In contrast, the region south of the caldera displays a well-defined low-velocity anomaly that extends southward into the Koa'e fault system. This north–south asymmetry reverses at 0 km depth (Figure 6d), where lower velocities are resolved beneath the northern summit and higher velocities beneath the southern summit.

At the 0.5 and 1 km depth layers (Figures 6e and 6f), the most prominent feature is a localized low-V_p anomaly east of Halema'uma'u crater, inside the caldera boundary. This anomaly remains distinct across both depth slices and marks the eastern margin of a low-velocity zone that persists over this depth interval, although its amplitude and lateral extent vary with depth in the cross-sections presented below. At depths of 2–3 km (Figures 6g and 6h), similar structural patterns persist, although the amplitude of the velocity contrasts is reduced. The central summit region remains slower than the surrounding flanks, while higher velocities become increasingly prominent north and east of the caldera margins. At 3 km depth, low-V_p anomalies dominate west of the caldera and extend southward toward the Koa'e fault system, emphasizing the lateral continuity of reduced velocities in this sector. Velocity gradients are strongest near the caldera walls and decrease with depth. At 4 km depth (Figure 6i), a northwest–southeast trending high-velocity feature is observed near the edge of the resolved region and should therefore be interpreted with caution.

5.2. *S*-Wave Velocity Model

The final V_s model provides complementary constraints on shear-wave velocity structure beneath the summit region of Kīlauea, with reliable resolution primarily between approximately −1 and 4 km depth, interrupted by

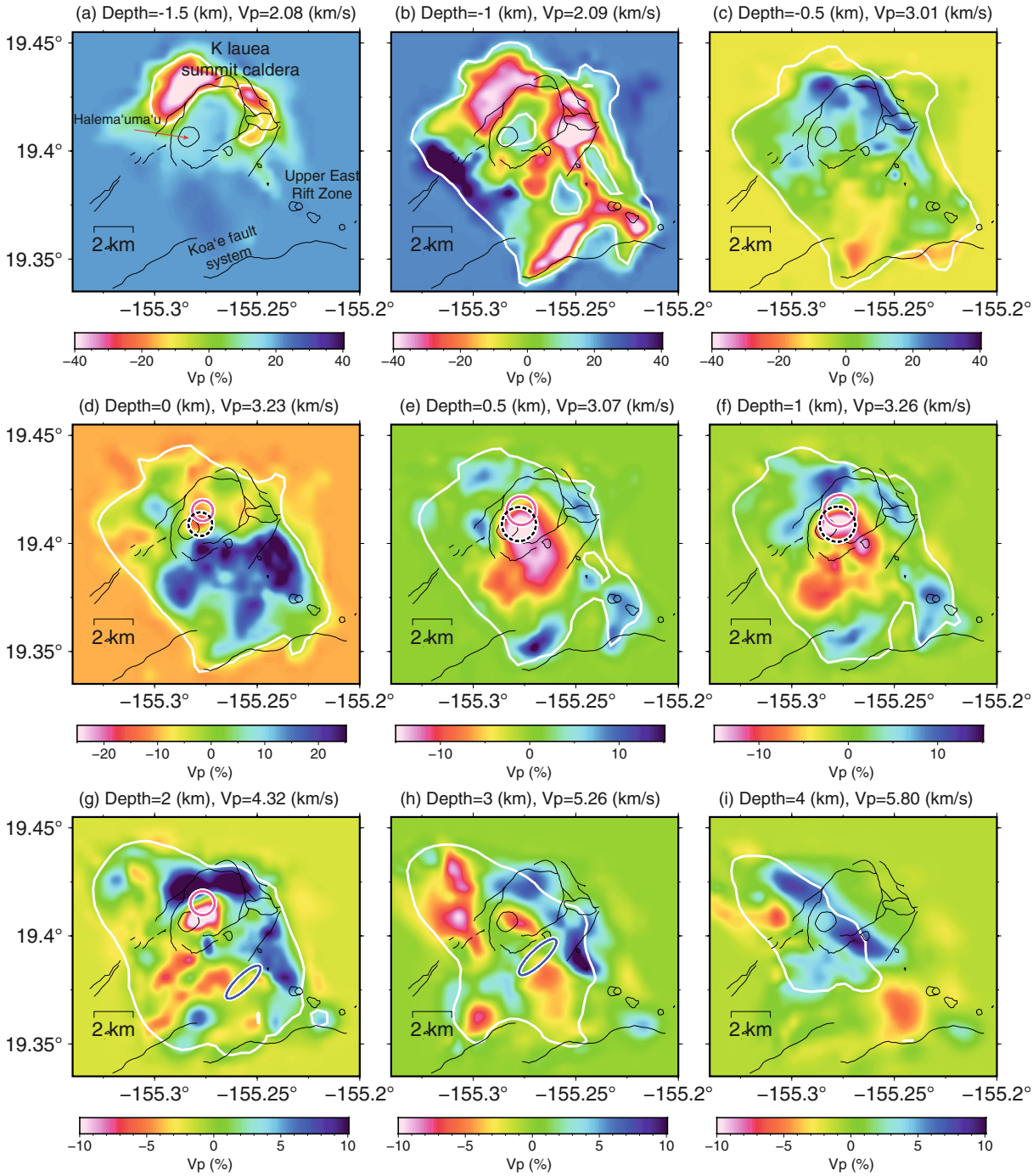


Figure 6. Horizontal slices of the V_p model beneath the summit of Kīlauea from −1.5 to 4 km depth relative to mean sea level. White contours mark the 0.3 resolution threshold. Geographic features are labeled in panel (a). Each panel shows V_p as a percentage perturbation relative to a reference velocity indicated at the top of the panel. The percentage color-scale range is larger for the shallow layers, where velocity variations are greatest. Pink and blue ellipses mark the geodetically modeled Halema'uma'u and south-caldera magma reservoirs of T. Wang et al. (2021), respectively, and the black dashed ellipse marks the Halema'uma'u reservoir inferred by Anderson et al. (2019). Each outline is the horizontal cross-section of the modeled source at the depth of that slice, so its size varies between panels, and outlines are drawn only on the slices their source intersects. The Halema'uma'u outline of T. Wang et al. (2021) therefore appears on the 0–2 km slices (panels d–g) and that of Anderson et al. (2019) on the 0–1 km slices (panels d–f). The south-caldera outline appears on the 2 and 3 km slices (panels g and h), and its lateral shift between them reflects the northwest dip of the modeled sill. Here V_p is compressional-wave velocity.

21699356, 2026, 10, Downloaded from https://agupubs.onlinelibrary.wiley.com/doi/10.1029/2026JB034515 by Capes, Wiley Online Library on [04/11/2026]. See the Terms and Conditions (https://onlinelibrary.wiley.com/terms-and-conditions) on Wiley Online Library for rules of use; OA articles are governed by the applicable Creative Commons License

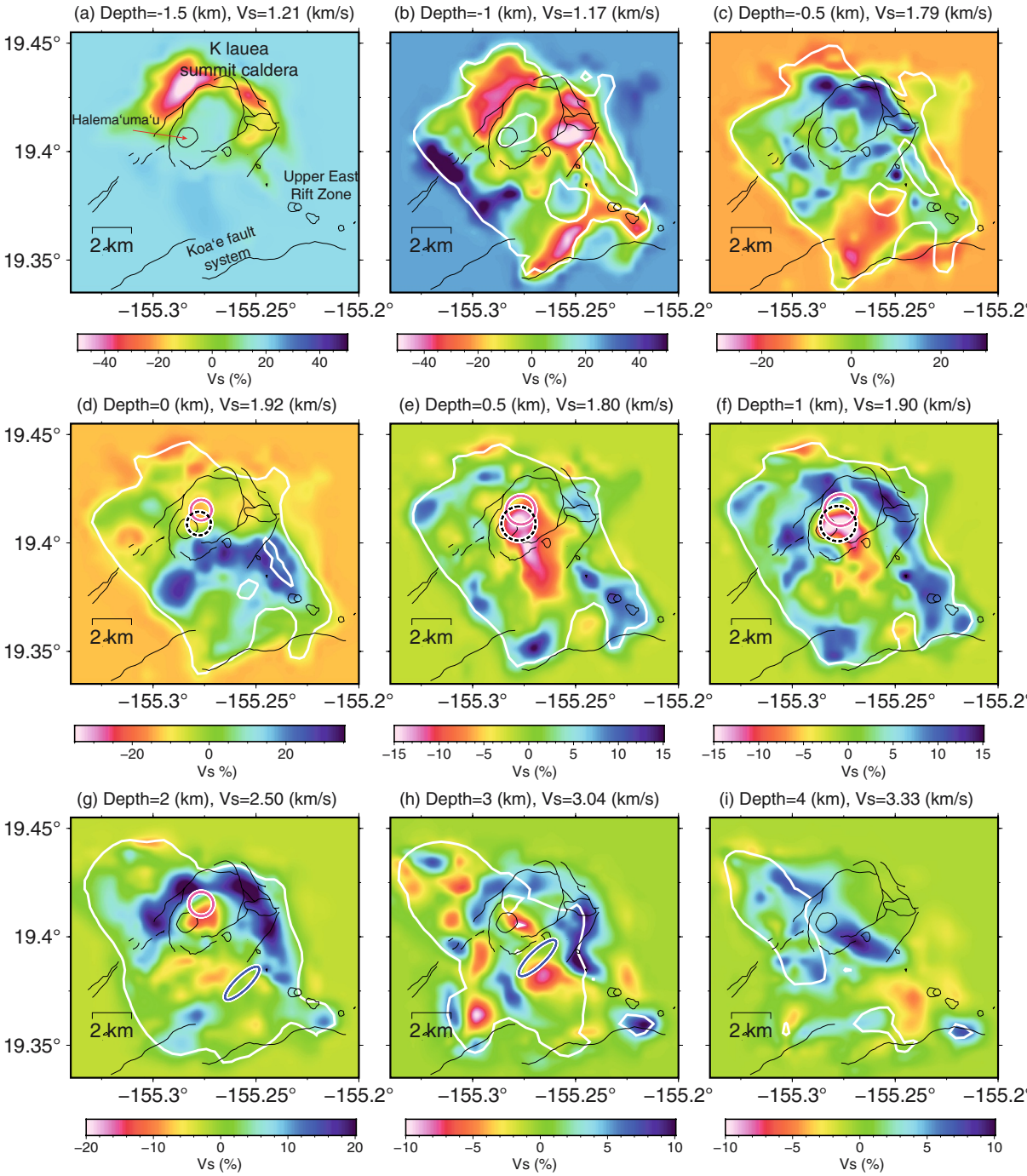


Figure 7. Horizontal slices of the V_s model beneath the summit of Kīlauea from −1.5 to 4 km depth relative to mean sea level (MSL). Each panel shows V_s as a percentage perturbation relative to a reference velocity indicated at the top of the panel. White contours mark the 0.3 resolution threshold, and geographic features are labeled in panel (a). Pink and blue ellipses mark the geodetically modeled Halema'uma'u and south-caldera magma reservoirs of T. Wang et al. (2021), respectively, and the black dashed ellipse marks the Halema'uma'u reservoir inferred by Anderson et al. (2019). Each outline is the horizontal cross-section of the modeled source at the depth of that slice, so its size varies between panels, and outlines are drawn only on the slices their source intersects. Depths are relative to MSL. Here V_s is shear-wave velocity.

the same 0–0.5 km minimum seen in V_p (Figure 7). At −1 km depth, low-V_s patches are concentrated around the summit caldera, with particularly prominent low-V_s structure along the caldera margins and toward the Upper East Rift Zone, while higher V_s occupies parts of the surrounding summit region. At −0.5 km depth, high-V_s anomalies dominate much of the summit caldera and extend into the East Rift Zone, with the strongest high-V_s

21699356, 2026, 10, Downloaded from https://agupubs.onlinelibrary.wiley.com/doi/10.1029/2026JB034515 by Capes, Wiley Online Library on [04/11/2026]. See the Terms and Conditions (https://onlinelibrary.wiley.com/terms-and-conditions) on Wiley Online Library for rules of use; OA articles are governed by the applicable Creative Commons License

values concentrated along the northern boundary of the caldera. In contrast, a pronounced low-V_s zone extends from the southern caldera margin toward the Koa'e fault system, forming a sharp north–south velocity gradient across the summit region. At 0 km depth, low-V_s anomalies dominate much of the summit caldera, forming a broad low-velocity region within the caldera interior. Outside the caldera, particularly to the south and east, very high-V_s anomalies are resolved, producing strong velocity contrasts across the caldera boundary.

From 0.5 to 1 km depth, the low-V_s structure becomes more focused, with the strongest reductions centered within the caldera, including a pronounced low-V_s anomaly east of Halema'uma'u. Surrounding regions show comparatively higher V_s, emphasizing strong lateral contrasts at these depths. At 2 km depth, a coherent low-V_s core persists beneath the summit, while by 3 km depth the low-V_s anomalies weaken and become more localized, consistent with reduced resolving power at greater depth. At 4 km depth, high-V_s structure is apparent beneath the summit caldera, while comparatively lower V_s anomalies occur along the Upper East Rift Zone. However, given the reduced resolution at this depth, these patterns are interpreted with caution.

Overall, the V_s model exhibits pronounced lateral variations within the upper 2–3 km that broadly correspond to features observed in the V_p model. Given the sensitivity of shear-wave velocities to temperature, melt fraction, fluid content, and rock damage in volcanic crust, the V_s structure provides complementary constraints on the physical state of the shallow summit system.

5.3. V_p/V_s Model

The final V_p/V_s model reveals spatially variable velocity-ratio structure across the summit region of Kīlauea, with reliable resolution over two separate depth intervals, −1 to −0.5 km and 1 to 4 km (Figure 8). Recovery is strongest between 2 and 3 km depth and falls away below 4 km, following the distribution of high-quality *S*-wave arrivals from tomographic earthquakes. The intervening 0–0.5 km interval is not recovered by the checkerboard, so V_p/V_s features confined to it are not interpreted, nor are structures below 4 km depth or near the model margins.

No coherent V_p/V_s structure is recovered at −1.5 km depth owing to the lack of usable *S*-wave constraints. At −1 km depth, the highest V_p/V_s values occur in the western portion of the summit region, whereas lower ratios are imaged along the northern margin. A broad zone of reduced V_p/V_s is also present south of the caldera and along the Upper East Rift Zone. At −0.5 km depth, the lowest ratios are concentrated south of the caldera, forming a laterally continuous anomaly that is bounded to the east by higher-ratio regions. The same anomaly is present again at 1 km depth. Because the intervening 0 and 0.5 km layers are not resolved for V_p/V_s, we treat these as two resolved expressions of the feature rather than as evidence of vertical continuity through that interval.

At 1 km depth, low V_p/V_s values are observed outside of the caldera in both the southwest and southeast sectors, whereas at 2 km depth, very low V_p/V_s values are imaged along the western and eastern margins of the summit caldera. These edge-aligned anomalies correspond to sharp lateral transitions in the V_p and V_s models and persist across multiple depth slices. A particularly coherent low-ratio anomaly west of the caldera remains evident at 3 km depth, where it spatially overlaps low-V_p and low-V_s anomalies. Additional low-V_p/V_s anomalies are also present farther south on the flank toward the Koa'e fault system. A weak expression of the anomaly is also present at 4 km depth, near the lower limit of reliable V_p/V_s recovery, and we therefore treat it with caution. The vertical structure of these map-view anomalies, and their integration into a conceptual model of the summit plumbing system, are examined in the vertical cross-sections presented next.

5.4. V_p, V_s, and V_p/V_s Cross-Sections

The cross-sections show that summit velocity structure is strongly depth-dependent: a laterally extensive high-velocity layer near sea level overlies localized low-V_p and low-V_s zones beneath Halema'uma'u and the south caldera that are laterally distinct at shallow levels and merge into a broader region of reduced velocity at greater depth. Figures 9 and 10 show vertical cross-sections of the final V_p, V_s, and V_p/V_s models across the summit region of Kīlauea, with north–south profiles (1-1′ to 4-4′) and west–east and oblique profiles (A-A′, B-B′, C-C′, and d-d′), respectively. Together, these sections provide a 3-D view of the summit plumbing system and illuminate strong lateral and vertical heterogeneity in the upper crust that is not readily apparent from map-view slices

21699356, 2026, 10, Downloaded from https://agupubs.onlinelibrary.wiley.com/doi/10.1029/2026JB034515 by Capes, Wiley Online Library on [04/11/2026]. See the Terms and Conditions (https://onlinelibrary.wiley.com/terms-and-conditions) on Wiley Online Library for rules of use; OA articles are governed by the applicable Creative Commons License

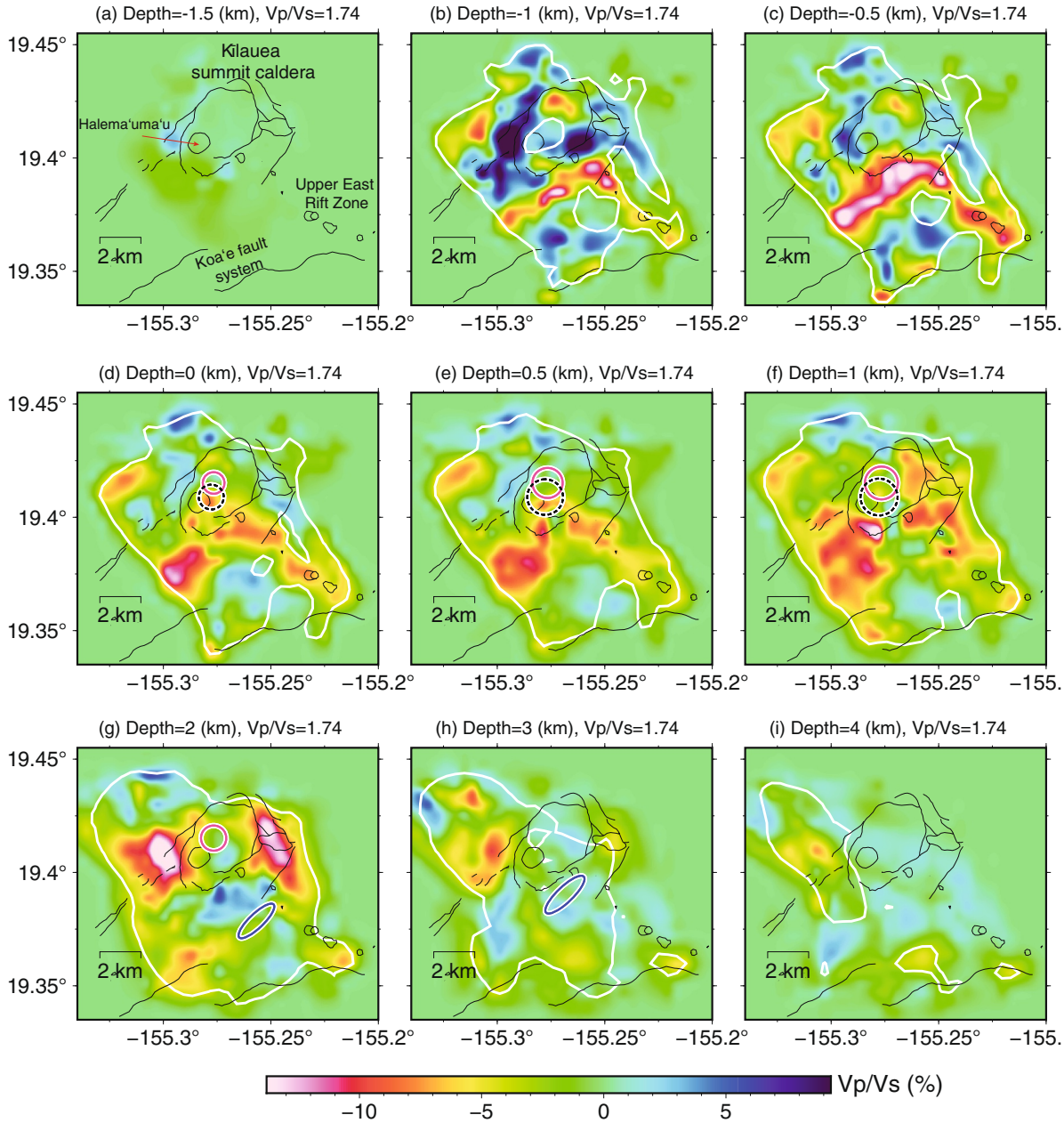


Figure 8. Horizontal slices of the V_p/V_s model beneath the summit of Kīlauea from −1.5 to 4 km depth relative to mean sea level (MSL). V_p/V_s is shown as a percentage perturbation relative to the reference ratio of 1.74 (the initial-model value, indicated at the top of each panel), on a single common color scale across all depths rather than the per-panel scales used in Figures 6 and 7. White contours mark the 0.3 resolution threshold, and geographic features are labeled in panel (a). Pink and blue ellipses mark the geodetically modeled Halema'uma'u and south-caldera magma reservoirs of T. Wang et al. (2021), respectively, and the black dashed ellipse marks the Halema'uma'u reservoir inferred by Anderson et al. (2019). Each outline is the horizontal cross-section of the modeled source at the depth of that slice, so its size varies between panels, and outlines are drawn only on the slices their source intersects. Depths are relative to MSL. Here V_p is compressional-wave velocity, V_s is shear-wave velocity, and V_p/V_s is the ratio of the two.

alone. The cross-sections are shown as percentage perturbations relative to the 1-D initial model. The corresponding absolute-velocity versions are provided (Figures S16 and S17 in Supporting Information S1).

The north–south profiles (1-1′ to 4-4′; Figure 9) reveal pronounced lateral heterogeneity across the summit region. Within the shallowest interval in which both models are resolved, from approximately −1 to −0.5 km depth, both V_p and V_s exhibit predominantly high-velocity anomalies beneath much of the caldera. This shallow high-velocity layer is laterally extensive and contrasts with lower velocities observed above and below this depth range.

21699356, 2026, 10, Downloaded from https://agupubs.onlinelibrary.wiley.com/doi/10.1029/2026JB034515 by Capes, Wiley Online Library on [04/11/2026]. See the Terms and Conditions (https://onlinelibrary.wiley.com/terms-and-conditions) on Wiley Online Library for rules of use; OA articles are governed by the applicable Creative Commons License

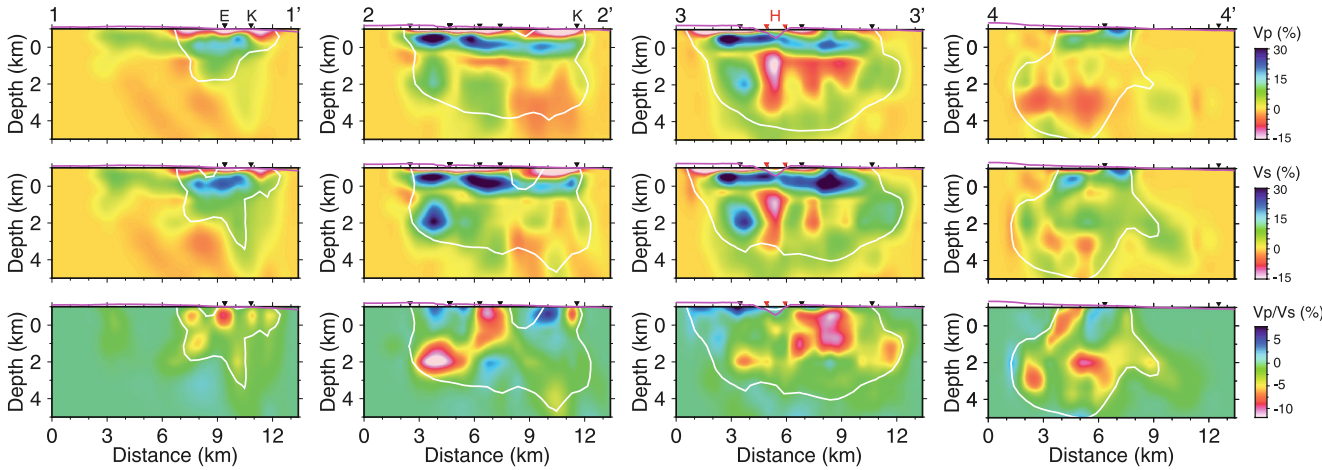


Figure 9. North–south vertical cross-sections of the V_p (top row), V_s (middle row), and V_p/V_s (bottom row) models, shown as percentage perturbations relative to the one-dimensional (1-D) initial model. Each column is one profile, labeled above the panels, and the three color scales at the right apply to the V_p, V_s, and V_p/V_s rows, respectively. Profiles correspond to the pink lines shown in Figure 3c. White contours mark the 0.3 resolution threshold, and a magenta line indicates surface topography. Depths are relative to mean sea level. Triangles at the top of every panel mark where each profile intersects the caldera rim and other major geologic features, with the labels given only on the V_p row. Red triangles along profile 3-3′ denote the boundaries of Halema'uma'u. Abbreviations: E, Upper East Rift Zone; K, Koa'e fault system; and H, Halema'uma'u. The corresponding absolute-velocity sections are shown in Figure S16 in Supporting Information S1. Here V_p is compressional-wave velocity, V_s is shear-wave velocity, and V_p/V_s is the ratio of the two.

Below about 1 km depth, velocity structure becomes more variable. Localized low-V_p and low-V_s zones emerge beneath portions of the caldera and toward the southern summit adjacent to the Koa'e fault system, producing clear north–south gradients within the upper 2–3 km. These gradients are most evident in the central profiles (2-2′ and 3-3′), where higher velocities north of the caldera transition to lower velocities toward the southern margin. At depths greater than approximately 2–3 km, anomalies become more localized, their amplitudes diminish within the resolved volume, and the structure appears comparatively smoother. The V_p/V_s sections show ratio anomalies in discrete shallow and mid-crustal zones that weaken below about 4 km.

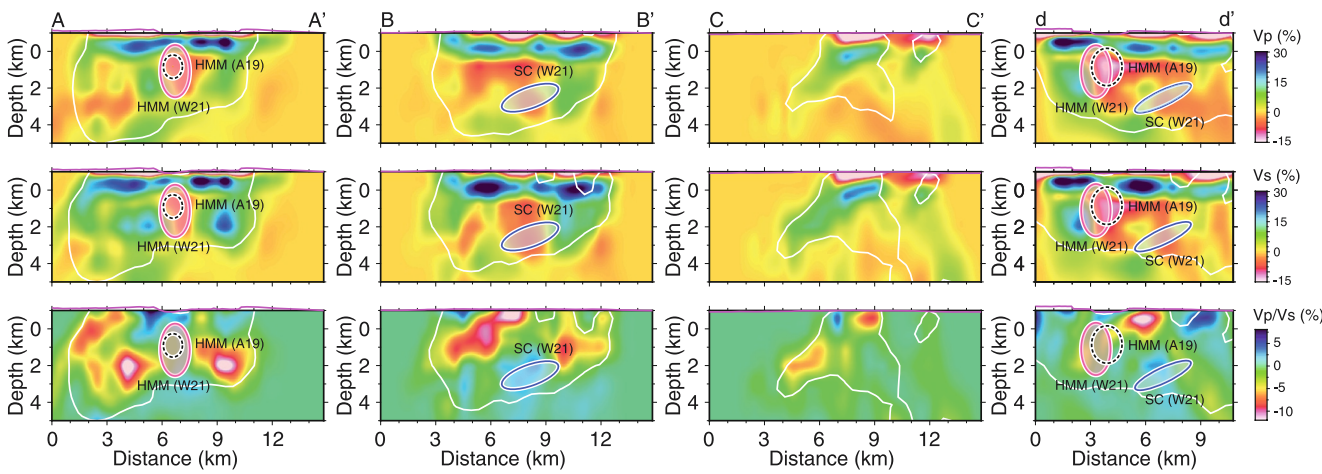


Figure 10. West–east and oblique vertical cross-sections of the V_p (top row), V_s (middle row), and V_p/V_s (bottom row) models along profiles A-A′, B-B′, C-C′, and d-d′, shown as percentage perturbations relative to the one-dimensional (1-D) initial model, with one profile per column, labeled above the panels. Profiles A-A′, B-B′, C-C′, and d-d′ are those shown in Figure 3c. Profiles A-A′ and B-B′ cross the geodetically modeled Halema'uma'u and south-caldera reservoirs, respectively, while the northwest–southeast profile d-d' intersects both. Pink and blue ellipses denote the cross-sectional projections of the Halema'uma'u and south-caldera magma reservoirs of T. Wang et al. (2021), labeled HMM (W21) and SC (W21) in the panels, and the black dashed ellipse denotes the Halema'uma'u reservoir inferred by Anderson et al. (2019), labeled HMM (A19). The corresponding absolute-velocity sections are shown in Figure S17 in Supporting Information S1. White contours mark the 0.3 resolution threshold, a magenta line indicates surface topography, and depths are relative to mean sea level. Here V_p is compressional-wave velocity, V_s is shear-wave velocity, and V_p/V_s is the ratio of the two.

21699356, 2026, 10, Downloaded from https://agupubs.onlinelibrary.wiley.com/doi/10.1029/2026JB034515 by Capes, Wiley Online Library on [04/11/2026]. See the Terms and Conditions (https://onlinelibrary.wiley.com/terms-and-conditions) on Wiley Online Library for rules of use; OA articles are governed by the applicable Creative Commons License

21699356, 2026, 10, Downloaded from https://agupubs.onlinelibrary.wiley.com/doi/10.1029/2026JB034515 by Capes, Wiley Online Library on [04/11/2026]. See the Terms and Conditions (https://onlinelibrary.wiley.com/terms-and-conditions) on Wiley Online Library for rules of use; OA articles are governed by the applicable Creative Commons License

The west–east and oblique profiles (A-A′, B-B′, C-C′, and d-d′; Figure 10) image the summit reservoir system in cross-section. Profiles A-A′ and B-B′ intersect the geodetically modeled Halema'uma'u and south-caldera reservoirs of T. Wang et al. (2021) and the Halema'uma'u reservoir of Anderson et al. (2019), and the oblique profile d-d′ crosses both. Near sea level, between about −1 and −0.5 km depth, profiles A-A′, B-B′, and d-d′ show predominantly high V_p and V_s beneath the caldera, consistent with the north–south sections, whereas profile C-C′, which lies south of the modeled reservoirs, shows more variable shallow structure and weaker contrasts at greater depth. Below this layer, profiles A-A′ and B-B′ image pronounced low-V_p and low-V_s anomalies at the modeled reservoirs. Beneath Halema'uma'u on profile A-A′, the anomaly is centered near 1–2 km depth and falls within the outline of Anderson et al. (2019). On profile B-B′, the anomaly lies at about 1–2 km depth, immediately updip and northwest of the south-caldera body, whose outline spans roughly 2–3 km depth and overlaps the anomaly along its shallow margin. The oblique profile d-d′ captures both features along a single section. Elevated V_p/V_s accompanies these low velocities in the upper 2–3 km near the reservoirs, though it is patchier and more laterally variable than the velocity anomalies themselves. At depths greater than about 3 km, velocity contrasts weaken and become more diffuse within the resolved volume.

Overall, the cross-sections highlight strong shallow heterogeneity beneath the summit. Both V_p and V_s show a high-velocity layer near sea level, underlain by more localized low-velocity zones at depths of approximately 1–3 km. Lateral contrasts are particularly evident across the caldera and toward the Koa'e fault system, but the pattern varies with depth and profile orientation. The northern and southern summit regions exhibit different velocity characteristics at specific depth intervals, although these differences are not uniform throughout the crust. This depth-dependent asymmetry provides an observational framework for interpreting magma storage and possible transfer pathways discussed in the conceptual model of magma storage and transport developed later in the Discussion.

6. Discussion

The final 3-D V_p, V_s, and V_p/V_s models provide an unprecedented view of the shallow summit structure of Kīlauea, parameterized on a 500 m grid, with recovery demonstrated at the sub-kilometer to kilometer scale. By integrating ultra-dense nodal seismic observations, active-source vibroseis data, and a carefully selected tomographic earthquake catalog, the inversion resolves pronounced lateral and vertical heterogeneity throughout the upper ∼4 km of the crust. The inclusion of both compressional- and shear-wave constraints allows the velocity structure to be examined not only in terms of bulk elastic properties (V_p), but also in quantities that are particularly sensitive to temperature, melt fraction, volatile content, and mechanically weak zones (V_s and V_p/V_s). Together, these models provide a more physically informative representation of the summit magma system than has been possible with previous data sets.

The resolved heterogeneity reflects the combined influences of magma storage and transport, volatile accumulation, hydrothermal alteration, and mechanical segmentation imposed by caldera-bounding faults, intrusive margins, and rift-related structures. These influences vary sharply over short distances, producing strong velocity gradients that delineate mechanically weak, melt- or fluid-rich domains from stronger, more competent crust. In this section, we first evaluate the robustness of the final velocity models using independent validation metrics, then synthesize the key structural features revealed by the V_p, V_s, and V_p/V_s models, compare them with prior studies, and discuss their implications for summit evolution, magma transport, and eruption forecasting at Kīlauea.

6.1. Model Validations

6.1.1. Travel-Time Residual Reductions

The effectiveness of the final 3-D velocity models is demonstrated by systematic reductions in travel-time residuals relative to the 1-D initial model (Figure S18 in Supporting Information S1). For both the active-source and earthquake data sets, the inversion substantially tightens the residual distributions while maintaining mean residuals close to zero. This behavior indicates a significant improvement in predictive accuracy without introducing systematic timing bias and provides a quantitative measure of how well the 3-D models capture the dominant velocity heterogeneity beneath the summit.

21699356, 2026, 10, Downloaded from https://agupubs.onlinelibrary.wiley.com/doi/10.1029/2026JB034515 by Capes, Wiley Online Library on [04/11/2026]. See the Terms and Conditions (https://onlinelibrary.wiley.com/terms-and-conditions) on Wiley Online Library for rules of use; OA articles are governed by the applicable Creative Commons License

For the active-source data set, residuals from shot-generated P arrivals improve from a mean of 0.135 s with a median absolute deviation (MAD) of 0.205 s in the 1-D initial model to a mean of 0.013 s and a MAD of 0.142 s in the final 3-D model, corresponding to a 31% reduction in MAD. Although this improvement is more modest than that observed for earthquake arrivals, it likely reflects the strong influence of near-surface heterogeneity on short-offset ray paths and the absence of corresponding S arrivals from the vibroseis sources, which limits joint constraints on shallow structure. Residual reductions for the earthquake data set are more pronounced. Residuals from tomographic-event P arrivals improve from a mean of 0.009 s and MAD of 0.143 s to 0.003 s and 0.056 s, respectively, representing a 61% reduction in MAD. Similarly, residuals from tomographic-event S arrivals improve from a mean of −0.028 s and MAD of 0.233 s to a mean of 0.009 s and MAD of 0.095 s, corresponding to a 59% reduction.

In the 1-D initial model, the near-zero mean residuals for the tomographic events indicate that the initial model provides a reasonable first-order approximation to the average velocity structure beneath the summit. The substantial reductions in MAD achieved by the 3-D inversion therefore reflect a genuine decrease in residual scatter associated with unmodeled lateral heterogeneity rather than compensation for large-scale bias. Following inversion, mean residuals for all data sets remain close to zero, generally within approximately 0.015 s, demonstrating that overall timing balance is preserved while the fit to individual arrivals is significantly improved. The larger improvement for tomographic-earthquake P arrivals relative to shot P arrivals likely reflects differences in ray-path sampling and source geometry. Shot arrivals primarily sample the shallowest parts of the crust where short-wavelength and relatively high-amplitude heterogeneity is more prevalent and more difficult to represent within the tomographic parameterization. In contrast, earthquake arrivals sample a broader depth range and provide more uniform coverage of deeper structure. In addition, earthquake hypocenters and origin times are solved for during the inversion, whereas shot locations and origin times are fixed, which naturally allows greater residual reduction for earthquake arrivals. Although P arrivals dominate the data set in both quantity and quality, the substantial improvement in S arrivals confirms the stability of the jointly inverted V_p and V_p/V_s models and supports the reliability of the inferred V_s structure within the well-resolved depth range. Collectively, these reductions indicate that the final models capture the principal 3-D velocity heterogeneity beneath the summit and yield markedly improved travel-time predictions for both passive and active sources.

6.1.2. Source Relocation Tests for the V_p Model

An independent and physically intuitive validation of the final V_p model is provided by relocation tests using the active vibroseis shots. In this analysis, shot locations are treated as unknown earthquake sources and relocated using both the 1-D initial model and the final 3-D V_p model. Because the vibroseis source locations are known with high precision, the resulting relocation errors directly quantify how well each velocity model reproduces the observed ray geometry and travel times in a complex volcanic environment.

Relocations using the 1-D initial model exhibit substantial errors, particularly in depth. Horizontal misfits are broadly distributed, with Δx ranging from −1,380 to 2,976 m and Δy ranging from −1,909 to 4,029 m (Figure 11a). Corresponding error statistics are shown in Figures S19a and S19b in Supporting Information S1, with mean values of −65 m (Δx) and 81 m (Δy), and MAD values of 220 and 485 m, respectively. Although the mean horizontal offsets are small, indicating no strong systematic bias, the broad scatter, particularly in Δy, highlights substantial unmodeled lateral heterogeneity in the north–south direction beneath the summit. Depth errors dominate the misfit, with Δz ranging from −4 to 2,383 m (Figure 11b), and a mean of 1,866 m (MAD 237 m; Figure S19c in Supporting Information S1). In one case, a source is relocated above the ground surface (not shown), underscoring the inadequacy of a 1-D approximation even under dense ray coverage.

In contrast, relocations using the final 3-D V_p model show dramatically improved accuracy in all components. Horizontal offsets are tightly clustered, with Δx ranging from −215 to 2,535 m (Figure 11c), and the majority of sources located within 100 m of their true positions (mean 24 m, MAD 69 m; Figure 11e and Figure S19d in Supporting Information S1). Similarly, Δy spans −642 to 1,654 m, with most offsets within 100 m (mean −4 m, MAD 59 m; Figure 11e and Figure S19e in Supporting Information S1). Vertical misfits are also substantially reduced, with Δz values between 3 and 2,049 m and the majority confined within 400 m (mean 200 m, MAD 92 m; Figure 11f and Figure S19f in Supporting Information S1). All Δz values are positive because relocated sources are necessarily positioned beneath the ground surface, consistent with the true vibroseis source geometry. The two sources with the largest errors ($\Delta x > 1.5$ km; red circles in Figure 11c) both lie at the far western margin

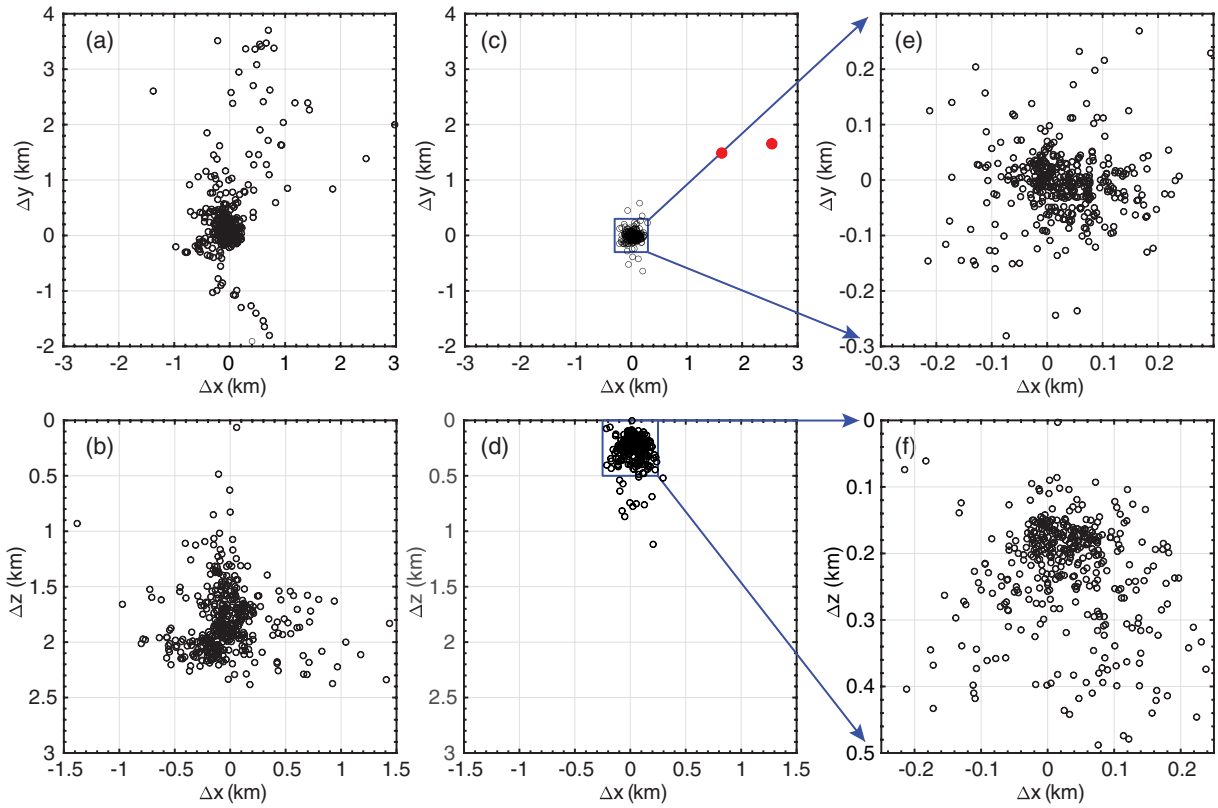


Figure 11. Independent ground-truth validation of the final V_p model using relocation of the vibroseis sources, whose true locations are known. (a) Δx versus Δy using the one-dimensional (1-D) initial model. (b) Δx versus Δz using the 1-D initial model. (c) Δx versus Δy using the three-dimensional (3-D) V_p model. (d) Δx versus Δz using the 3-D V_p model. (e, f) Enlarged views of the regions highlighted in (c) and (d). Scales are matched between panels to allow direct comparison. Positive Δx indicates westward shifts, positive Δy indicates northward shifts, and Δz is positive for all sources relocated in the 3-D model, which lie beneath the ground surface. Red circles in panel (c) mark the two sources with the largest relocation errors ($\Delta x > 1.5$ km), both located at the far western edge of the array where ray-path coverage is one-sided. They lie outside the plotted Δx range of panels (b), (d), (e), and (f). Here V_p is compressional-wave velocity.

of the array, where ray-path coverage is strongly one-sided. Excluding these two edge sources, the largest remaining Δx is under 300 m, confirming that the elevated maximum offsets are confined to the array periphery.

Map-view patterns of relocation error (Figure S20 in Supporting Information S1) show that the largest offsets occur near the edges of the array, where ray-path coverage is sparser and crossing geometries are less favorable. All sources lie within the region enclosed by the resolution contour (pink line in Figure S20d in Supporting Information S1), and the largest misfits occur along the margins of that region, where ray coverage is weakest, rather than in the well-resolved core beneath the summit. Within the central summit region, where station density and ray-path overlap are highest, relocations are markedly more accurate. This spatial dependence closely mirrors the checkerboard resolution results and reinforces the conclusion that the resolved velocity structure is most reliable beneath the core of the experiment.

Because *S*-wave arrivals are not available for the vibroseis sources, this validation is necessarily limited to the V_p model. Inclusion of *S*-wave constraints would likely further improve depth control, particularly in the shallow crust. Nevertheless, given the strong near-surface heterogeneity at Kīlauea, the remaining mislocations likely represent an upper bound on achievable accuracy under the present geometry. Overall, the relocation tests provide independent confirmation that the 3-D V_p model substantially improves source-location accuracy relative to the 1-D initial model by explicitly accounting for lateral velocity heterogeneity beneath the summit. This improvement underscores the value of the final velocity models for high-precision earthquake locations, real-time seismic monitoring, and hazard assessment at Kīlauea. Formal uncertainties for natural earthquakes are only statistical estimates conditioned on an assumed velocity model, since the true hypocenters are unknown. The

21699356, 2026, 10, Downloaded from https://agupubs.onlinelibrary.wiley.com/doi/10.1029/2026JB034515 by Capes, Wiley Online Library on [04/11/2026]. See the Terms and Conditions (https://onlinelibrary.wiley.com/terms-and-conditions) on Wiley Online Library for rules of use; OA articles are governed by the applicable Creative Commons License

21699356, 2026, 10, Downloaded from https://agupubs.onlinelibrary.wiley.com/doi/10.1029/2026JB034515 by Capes, Wiley Online Library on [04/11/2026]. See the Terms and Conditions (https://onlinelibrary.wiley.com/terms-and-conditions) on Wiley Online Library for rules of use; OA articles are governed by the applicable Creative Commons License

vibroseis shots have known locations and thus give an absolute measure of location accuracy, so we base this test on them.

6.2. Relation to Prior Tomographic and Complementary Geophysical Studies

Seismic tomography has played a central role in shaping the current understanding of magma storage and transport beneath Kīlauea and the Island of Hawai'i. Early regional-scale studies consistently imaged broad low-velocity anomalies beneath the summit and rift zones, establishing the existence of shallow magma storage and deeper rift-related pathways linking the summit to the East Rift Zone (e.g., Dawson et al., 1999; Okubo et al., 1997; Rowan & Clayton, 1993; Thurber, 1984, 1987). These foundational investigations demonstrated that the summit and rift systems are underlain by anomalously low velocities relative to surrounding crust, but their resolving power was limited by sparse station coverage and strongly uneven ray-path geometries.

Subsequent work using expanded earthquake catalogs and improved inversion strategies refined this picture by confirming laterally extensive low-V_p regions beneath the summit and rifts and by better delineating the depth extent of these anomalies (J. Got et al., 2006; J. L. Got et al., 2008; Haslinger et al., 2001; Monteiller et al., 2005; Park et al., 2007, 2009). Regional-scale body-wave tomography has resolved large-scale velocity structure beneath Kīlauea and the Island of Hawai'i, including variations in the lower crust and upper mantle that provide important boundary conditions for summit-scale interpretations (Syracuse et al., 2010; Wolfe et al., 2009). Nevertheless, resolution remained insufficient to robustly image narrow features, sharp velocity gradients, or vertically continuous structures within the shallowest few kilometers, where magma storage, withdrawal, and deformation are concentrated.

A significant advance was achieved with 3-D body-wave tomography that explicitly accounted for strong lateral heterogeneity through improved event relocation and inversion strategies (Lin, Shearer, et al., 2014). That study resolved sharper velocity contrasts beneath the summit and demonstrated that shallow low-velocity structure is more spatially complex than previously recognized. Related summit-focused tomographic analyses further emphasized the importance of fine-scale heterogeneity and the limitations imposed by permanent network geometry (e.g., Lin, Amelung, et al., 2014). Despite these improvements, the effective resolution of these models was still fundamentally constrained by station spacing and ray-path coverage.

The present study builds on this prior tomographic work by combining ultra-dense nodal coverage with both passive earthquake and active-source data, inverted on a 500 m grid. This hybrid tomographic approach enables imaging of sharp velocity gradients, resolution of vertically coherent low-V_p and low-V_s structures, and delineation of flanking higher-velocity regions that bound the summit interior at the sub-kilometer to kilometer scale. Compared to earlier tomographic models, the results more clearly distinguish laterally extensive background anomalies from localized, vertically organized features in the shallow crust.

Beyond seismology, independent geophysical studies provide complementary constraints on the summit structure. Ground magnetic, self-potential, and aeromagnetic surveys have mapped demagnetized and hydrothermally altered zones beneath the caldera (Davis, 2015; Gailler et al., 2024; Hildenbrand et al., 1993), and magnetotelluric imaging has identified shallow conductive regions interpreted to reflect fluids, alteration, and possible melt (Hoversten et al., 2022). The low V_p, low V_s, and locally elevated V_p/V_s anomalies imaged here are broadly co-located with these conductive and demagnetized zones, providing multi-method support for the presence of hot, fluid-rich, and possibly partially molten material beneath the summit.

In the following subsection, we synthesize these seismic and complementary geophysical observations to interpret the geometry and physical state of magma storage and transport beneath the summit. A formal joint inversion of these data sets is beyond the present scope.

6.3. Conceptual Architecture and Implications for Magma Transport

The fine spatial resolution of the seismic velocity models, enabled by the 500 m inversion grid, permits direct comparison with independent geodetic, geologic, and petrologic constraints on recent summit activity at Kīlauea. Of these complementary observations, surface deformation is particularly informative because it helps identify subsurface volumes undergoing pressure change during volcanic activity. The largest recent perturbation to the summit system occurred during the 2018 eruption, when withdrawal of about 1.5 km^3 dense rock equivalent of

21699356, 2026, 10, Downloaded from https://agupubs.onlinelibrary.wiley.com/doi/10.1029/2026JB034515 by Capes, Wiley Online Library on [04/11/2026]. See the Terms and Conditions (https://onlinelibrary.wiley.com/terms-and-conditions) on Wiley Online Library for rules of use; OA articles are governed by the applicable Creative Commons License

magma was accompanied by large-scale collapse of the summit of Kīlauea (Neal et al., 2019). The 2018 eruption ended abruptly on 4 August 2018 and was followed for nearly 300 days by simultaneous inflation beneath Halema'uma'u and deflation south of the caldera (T. Wang et al., 2021). Joint inversion of lava lake withdrawal, GPS, tilt, and InSAR data during the 2018 collapse sequence identified a shallow Halema'uma'u reservoir centered just east of Halema'uma'u crater at about 2 km beneath the surface, approximately 1 km below sea level (Anderson et al., 2019). Anderson et al. (2019) also noted residual subsidence south of the caldera that likely reflects early drainage from a deeper south-caldera storage region. In the post-2018 period, T. Wang et al. (2021) resolved two principal source regions: an inflating Halema'uma'u source whose location closely overlaps the 2018 reservoir of Anderson et al. (2019), and a south-caldera source represented by a thin ellipsoidal body (T. Wang et al., 2021). That source geometry was required to reproduce both the southeast-trending subsidence south of the caldera and the strong southeastward displacements within and surrounding that area of deformation (T. Wang et al., 2021). As shown in the map-view slices (Figures 6–8) and the reservoir-crossing cross-sections (Figure 10), these geodetically inferred source regions correspond closely to tomographic anomalies characterized by low V_p, low V_s, and locally elevated V_p/V_s beneath Halema'uma'u and the south caldera.

The correspondence between these geodetically inferred source regions and the tomographic velocity anomalies is consistent with the interpretation that the imaged structures are closely associated with the summit magma system. Tilt and GPS observations indicate that the anomalous volume beneath Halema'uma'u, defined by low V_p, low V_s, and locally elevated V_p/V_s, has repeatedly marked the locus of inflation and deflation during post-2018 eruptive episodes. During the 2018 eruption, deformation was dominated by withdrawal from the shallow Halema'uma'u reservoir modeled by Anderson et al. (2019), consistent with the large-scale summit collapse described by Neal et al. (2019). Following the eruption, the Halema'uma'u source resumed inflation even as the south-caldera source continued to deflate (T. Wang et al., 2021). The spatial correspondence between these distinct but temporally related deformation sources and the tomographic velocity structure in Figures 6–8 and 10 is direct beneath Halema'uma'u, where the imaged anomaly falls within the geodetic source outline, while beneath the south caldera the modeled outline overlaps the imaged low velocities along its shallow margin and extends downdip of them. Taken together, this correspondence supports the interpretation that the low-V_p and low-V_s anomalies, together with locally elevated V_p/V_s, define key parts of the Kīlauea summit magma system.

Taken together, the seismic and geodetic observations support a summit plumbing configuration in which the Halema'uma'u and south-caldera reservoirs occupy distinct but closely related parts of a broader shallow magmatic system. The depth-dependent continuity of low-V_s and low-V_p structure between the Halema'uma'u and south-caldera regions along profile d-d' (Figure 10), together with locally elevated V_p/V_s within these low-velocity regions, is consistent with structural linkage and possible magma-transfer pathways beneath the summit.

The resolution tests establish that the models recover sub-kilometer to kilometer-scale structure in the best-resolved parts of the summit region. Overall, these multidisciplinary comparisons indicate that V_s and V_p/V_s provide important constraints on the thermal, magmatic, and volatile state of the shallow plumbing system. The close correspondence between seismic and geodetic observations supports the interpretation of a shallow summit core in which low-velocity regions with locally elevated V_p/V_s may mark magma storage zones embedded within a broader structural framework that helps govern magma storage and transfer beneath Kīlauea.

Several limitations bear on these interpretations. First, the inversion assumes isotropic velocities, whereas seismic anisotropy can be significant in volcanic crust and, if neglected, may bias the recovered velocities and V_p/V_s. The models should therefore be understood as effective isotropic velocities (e.g., Araragi et al., 2015; Lo Bue et al., 2024). In addition, low velocities and elevated V_p/V_s are non-unique indicators: similar anomalies can arise from combinations of elevated temperature, partial melt, fluid saturation, hydrothermal alteration, fracturing, and volatile content, and the present data cannot uniquely separate these contributions. We therefore interpret the anomalies as consistent with magma storage rather than as unique evidence of melt, and the geodetic correspondence is presented as supporting evidence rather than direct validation of the reservoir geometry. Finally, the link between low velocities, elevated V_p/V_s, and melt remains qualitative here. Converting velocities and V_p/V_s into quantitative melt fractions would require thermodynamic and petrophysical modeling (e.g., MAGEMin; Riel et al., 2022), which we identify as a valuable direction for future work.

21699356, 2026, 10, Downloaded from https://agupubs.onlinelibrary.wiley.com/doi/10.1029/2026JB034515 by Capes, Wiley Online Library on [04/11/2026]. See the Terms and Conditions (https://onlinelibrary.wiley.com/terms-and-conditions) on Wiley Online Library for rules of use; OA articles are governed by the applicable Creative Commons License

6.4. Methodological Advances

Several methodological elements contributed directly to the resolution achieved in this study. Dense station spacing of approximately 100–200 m across the summit region enabled detailed sampling of shallow velocity heterogeneity and reduced spatial aliasing of short-wavelength structure. Automated phase picking using the STA/LTA, RESTX, and PhaseNet algorithms produced millions of consistent *P* and *S* arrivals, reducing subjective bias and improving timing consistency across the large data set. As detailed above, *P* arrivals were drawn primarily from RESTX and STA/LTA and *S* arrivals primarily from PhaseNet, with agreement among the methods used as a quality check and phase association performed within the RESTX framework. The integration of passive earthquake observations with active-source vibroseis data provided complementary ray-path geometries, combining dense short-offset coverage in the shallow crust with longer-offset paths that constrain deeper structure. A systematic tomographic-event selection strategy further ensured spatially distributed and well-constrained sources, stabilizing the inversion and limiting the influence of poorly constrained hypocenters. Together, these components improved path coverage, strengthened conditioning of the inverse problem, and enabled recovery of localized velocity anomalies and sharp lateral gradients that are difficult to resolve with permanent networks alone. The experiment demonstrates the value of large-scale nodal deployments for high-resolution imaging of active volcanic systems.

7. Conclusions

The dense nodal seismic experiment and hybrid passive-active data set presented here provide high-resolution images of the summit region of Kīlauea. By resolving V_p, V_s, and V_p/V_s structure at the sub-kilometer to kilometer scale, the resulting models illuminate the internal architecture of the summit plumbing system with substantially improved spatial detail. The velocity models image two primary shallow reservoir regions beneath Halema'uma'u and the south caldera, expressed as localized zones of reduced V_p and V_s and, in places, elevated V_p/V_s ratios. These anomalies are embedded within and defined by a heterogeneous structural framework characterized by laterally varying high-velocity domains that likely represent mechanically stronger intrusive complexes or coherent host rock.

Comparison with independent geodetic observations shows close spatial correspondence between seismic velocity anomalies and the modeled deformation sources, particularly beneath Halema'uma'u, supporting the interpretation that the imaged structures are consistent with magma storage regions. The enhanced expression of reservoir-scale anomalies in V_s and, to a lesser extent, V_p/V_s, underscores the sensitivity of shear-wave velocities and velocity ratios to temperature, melt fraction, and volatile content in the shallow basaltic crust. Resolving these features at the sub-kilometer to kilometer scale represents an advance in linking elastic properties to magmatic processes beneath an active basaltic volcano.

More broadly, this study demonstrates the feasibility and scientific value of combining ultra-dense nodal deployments with hybrid passive-active tomography for imaging shallow volcanic systems. The framework applied here, combining dense temporary deployments, automated phase detection, tomographic-event selection, and controlled-source integration, is transferable to other restless calderas where linking surface unrest to subsurface magma storage remains difficult. Resolving both the geometry and the elastic properties of reservoirs and their host rock can sharpen constraints on storage architecture, structural segmentation, and potential intrusion pathways. The resulting velocity models provide a physically grounded baseline against which future changes in seismic velocity, seismicity patterns, and deformation can be evaluated. As Kīlauea continues to evolve following the 2018 eruption, such high-resolution structural models provide an improved framework for interpreting magma storage and possible transfer between summit reservoirs, and for assessing how future intrusions or eruptions may initiate within the summit region. In this way, the 2023 Kīlauea experiment serves both as a detailed case study of an active volcanic system and as a template for next-generation seismic imaging of magmatic environments worldwide.

Conflict of Interest

The authors declare no conflicts of interest relevant to this study.

Availability Statement

The passive and active-source seismic waveforms used in this study are archived at the EarthScope Data Management Center under FDSN network code 6F (U.S. Geological Survey, 2023). The earthquake catalog and the *P*- and *S*-wave arrival times derived from those recordings are available from the U.S. Geological Survey ScienceBase repository (Roecker et al., 2026). The final 3-D V_p, V_s, and V_p/V_s models, the catalog of the 799 tomographic earthquakes used in the inversion, and the corresponding inversion input files are archived at Zenodo (Lin et al., 2026). The tomographic inversions were computed with the SIMUL2000 code (Thurber & Eberhart-Phillips, 2021). Automated phase picking used PhaseNet (Zhu & Beroza, 2019b) and the RESTX package (Comte et al., 2019). The figures were prepared with the Generic Mapping Tools (Wessel et al., 2019).

Acknowledgments

We thank the staff of the U.S. Geological Survey Hawaiian Volcano Observatory, Alaska Volcano Observatory, California Volcano Observatory, and Cascades Volcano Observatory for essential support with field deployment, logistics, and permitting. We are especially grateful to Hawai'i Volcanoes National Park for facilitating access, supporting helicopter operations, and helping ensure cultural and environmental sensitivity throughout the project. We acknowledge the EarthScope Primary Instrument Center (EPIC) and the Marian and Edward Erdelyi Science Fund for providing seismic nodes and the NHERI facility at the University of Texas at Austin for access to the T-Rex vibroseis truck. We thank Steven Brantley for leading permitting efforts, and Liliana DeSmither and Rebecca Kramer for logistical coordination. We thank the Associate Editor, three anonymous reviewers, and a USGS internal reviewer for their thorough and constructive comments, which substantially improved the manuscript. This project was supported by the Additional Supplemental Appropriations for Disaster Relief Act, 2019 (H.R. 2157), through the U.S. Geological Survey, and by National Science Foundation Grants EAR-2218645 (University of Miami), EAR-2218646 (Rensselaer Polytechnic Institute), and CMMI-2037900 (NHERI, UT-Austin). This work used Bridges-2 at the Pittsburgh Supercomputing Center through allocation ees240009p from the Advanced Cyberinfrastructure Coordination Ecosystem: Services & Support program (ACCESS, Boerner et al., 2023), which is supported by the National Science Foundation. Any use of trade, firm, or product names is for descriptive purposes only and does not imply endorsement by the U.S. Government.

References

Allen, R. V. (1978). Automatic earthquake recognition and timing from single traces. *Bulletin of the Seismological Society of America*, *68*(5), 1521–1532. https://doi.org/10.1785/bssa0680051521

Anderson, K. R., Johanson, I. A., Patrick, M. R., Gu, M., Segall, P., Poland, M. P., et al. (2019). Magma reservoir failure and the onset of caldera collapse at Kīlauea volcano in 2018. *Science*, *366*(6470), eaaz1822. https://doi.org/10.1126/science.aaz1822

Aoki, Y., Takeo, M., Aoyama, H., Fujimatsu, J., Matsumoto, S., Miyamachi, H., et al. (2009). P-wave velocity structure beneath Asama volcano, Japan, inferred from active source seismic experiment. *Journal of Volcanology and Geothermal Research*, *187*(3), 272–277. https://doi.org/10.1016/j.jvolgeores.2009.09.004

Araragi, K. R., Savage, M. K., Ohminato, T., & Aoki, Y. (2015). Seismic anisotropy of the upper crust around Mount Fuji, Japan. *Journal of Geophysical Research*, *120*(4), 2739–2751. https://doi.org/10.1002/2014jb011554

Auger, E., Gasparini, P., Virieux, J., & Zollo, A. (2001). Seismic evidence of an extended magmatic sill under Mt. Vesuvius. *Science*, *294*(5546), 1510–1512. https://doi.org/10.1126/science.1064893

Baker, S., & Amelung, F. (2012). Top-down inflation and deflation at the summit of Kilauea volcano, Hawaii observed with InSAR. *Journal of Geophysical Research*, *117*(B12406). https://doi.org/10.1029/2011jb009123

Baker, S., & Amelung, F. (2015). Pressurized magma reservoir within the east rift zone of Kīlauea volcano, Hawaii: Evidence for relaxed stress changes from the 1975 Kalapana earthquake. *Geophysical Research Letters*, 2015GL063161. https://doi.org/10.1002/2015GL063161

Boerner, T. J., Deems, S., Furlani, T. R., Knuth, S. L., & Towns, J. (2023). ACCESS: Advancing innovation: NSF's advanced cyberinfrastructure coordination ecosystem: Services & support. In *Practice and experience in advanced research computing, PEARC '23* (pp. 173–176). Association for Computing Machinery.

Cervelli, P., & Miklius, A. (2003). *The shallow magmatic system of Kilauea volcano* (Vol. 1676, pp. 149–163). U.S. Geological Survey Professional Paper.

Comte, D., Farias, M., Roecker, S., & Russo, R. (2019). The nature of the subduction wedge in an erosive margin: Insights from the analysis of aftershocks of the 2015 Mw 8.3 Illapel earthquake beneath the Chilean coastal range. *Earth and Planetary Science Letters*, *520*, 50–62. https://doi.org/10.1016/j.epsl.2019.05.033

Crosson, R. S., & Koyanagi, R. Y. (1979). Seismic velocity structure below the Island of Hawaii from local earthquake data. *Journal of Geophysical Research*, *84*(B5), 2331–2342. https://doi.org/10.1029/jb084ib05p02331

Dahlen, F. A., Hung, S. H., & Nolet, G. (2000). Fréchet kernels for finite-frequency traveltimes—I. Theory. *Geophysical Journal International*, *141*(1), 157–174. https://doi.org/10.1046/j.1365-246x.2000.00070.x

Davis, P. M. (2015). Geothermal evolution of an intruded dike in the rift zone of Kilauea volcano, Hawaii from VLF and self-potential measurements. *Journal of Volcanology and Geothermal Research*, *302*, 64–80. https://doi.org/10.1016/j.jvolgeores.2015.06.007

Dawson, P. B., Chouet, B. A., Okubo, P. G., Villaseñor, A., & Benz, H. M. (1999). Three-dimensional velocity structure of the Kilauea caldera, Hawaii. *Geophysical Research Letters*, *26*(18), 2805–2808. https://doi.org/10.1029/1999gl005379

Delaney, P., Fiske, R., Miklius, A., Okamura, A., & Sako, M. (1990). Deep magma body beneath the summit and rift zones of Kilauea volcano, Hawaii. *Science*, *247*(4948), 1311–1316. https://doi.org/10.1126/science.247.4948.1311

Denlinger, R., O'Connell, D., Lin, G., Roecker, S., & Bennington, N. (2024). An unprecedented experiment to map Kīlauea's summit magma system. *Eos*, *105*. https://doi.org/10.1029/2024eo240392

Dzurisin, D., Koyanagi, R. Y., & English, T. T. (1984). Magma supply and storage at Kilauea volcano, Hawaii, 1956–1983. *Journal of Volcanology and Geothermal Research*, *21*(3–4), 177–206. https://doi.org/10.1016/0377-0273(84)90022-2

Earle, P. S., & Shearer, P. M. (1994). Characterization of global seismograms using an automatic-picking algorithm. *Bulletin of the Seismological Society of America*, *84*(2), 366–376. https://doi.org/10.1785/bssa0840020366

Eaton, J. P., & Murata, K. J. (1960). How volcanoes grow. *Science*, *132*(3432), 925–938. https://doi.org/10.1126/science.132.3432.925

Eberhart-Phillips, D. (1986). Three-dimensional velocity structure in the northern California Coast ranges from inversion of local earthquake arrival times. *Bulletin of the Seismological Society of America*, *76*(4), 1025–1052.

Eberhart-Phillips, D. (1990). Three-dimensional P and S velocity structure in the Coalinga region, California. *Journal of Geophysical Research*, *95*(B10), 15343–15363. https://doi.org/10.1029/jb095ib10p15343

Eberhart-Phillips, D., & Michael, A. J. (2004). Seismotectonics of the Loma Prieta region determined from three-dimensional P-wave velocities, VP/VS ratios, and seismicity. *U.S. Geological Survey Professional Paper*, *1550-E*, E165–E187.

Eberhart-Phillips, D., Stanley, W. D., Rodriguez, B. D., & Lutter, W. J. (1995). Surface seismic and electrical methods to detect fluids related to faulting. *Journal of Geophysical Research*, *100*(B7), 12919–12936. https://doi.org/10.1029/94jb03256

Gailler, L., Bouligand, C., Kauahikaua, J., Lénat, J.-F., & Cluzel, N. (2024). The subsurface structure of the Kīlauea caldera before its 2018 collapse inferred from ground magnetic, SP, and temperatures anomalies. *Journal of Geophysical Research*, *129*(4), e2023JB028005. https://doi.org/10.1029/2023jb028005

Got, J., Monteiller, V., Virieux, J., & Okubo, P. (2006). Estimating crustal heterogeneity from double-difference tomography. *Pure and Applied Geophysics*, *163*(2–3), 405–430.

Got, J.-L., Monteiller, V., Monteux, J., Hassani, R., & Okubo, P. (2008). Deformation and rupture of the oceanic crust may control growth of Hawaiian volcanoes. *Nature*, *451*(7177), 453–456. https://doi.org/10.1038/nature06481

21699356, 2026, 10, Downloaded from https://agupubs.onlinelibrary.wiley.com/doi/10.1029/2026JB034515 by Capes, Wiley Online Library on [04/11/2026]. See the Terms and Conditions (https://onlinelibrary.wiley.com/terms-and-conditions) on Wiley Online Library for rules of use; OA articles are governed by the applicable Creative Commons License

Haslinger, F., Thurber, C., Mandernach, M., & Okubo, P. (2001). Tomographic image of P-velocity structure beneath Kilauea's east rift zone and south flank: Seismic evidence for a deep magma body. *Geophysical Research Letters*, *28*(2), 375–378. https://doi.org/10.1029/2000gl012018

Hildenbrand, T. G., Rosenbaum, J. G., & Kauahikaua, J. P. (1993). Aeromagnetic study of the Island of Hawaii. *Journal of Geophysical Research*, *98*(B3), 4099–4119. https://doi.org/10.1029/92jb02483

Hoversten, G. M., Gasperikova, E., Mackie, R., Myer, D., Kauahikaua, J., Newman, G. A., & Cuevas, N. (2022). Magnetotelluric investigations of the Kīlauea Volcano, Hawaii. *Journal of Geophysical Research*, *127*(8), e2022JB024418. https://doi.org/10.1029/2022jb024418

Ibáñez, J. M., Prudencio, J., Díaz-Moreno, A., Patanè, D., Puglisi, G., Lühr, B.-G., et al. (2016). The TOMO-ETNA experiment: An imaging active campaign at Mt. Etna volcano. Context, main objectives, working-plans and involved research projects. *Annales Geophysicae*, *59*(4), S0426. https://doi.org/10.4401/ag-7079

Janiszewski, H., Bennington, N., & Wight, J. (2024). A seismic nodal deployment to understand magmatic structure in the vicinity of the Pāhala earthquake swarm. *Seismological Research Letters*, *95*(5), 3082–3092. https://doi.org/10.1785/0220240060

Jones, J. P., & van der Baan, M. (2015). Adaptive STA–LTA with outlier statistics. *Bulletin of the Seismological Society of America*, *105*(3), 1606–1618. https://doi.org/10.1785/0120140203

Klein, F. W. (1981). A linear gradient crustal model for south Hawaii. *Bulletin of the Seismological Society of America*, *71*(5), 1503–1510. https://doi.org/10.1785/bssa0710051503

Klein, F. W., Koyanagi, R. Y., Nakata, J. S., & Tanigawa, W. R. (1987). The seismicity of Kilauea's magma system. *U.S. Geological Survey Professional Paper*, *1350*, 1019–1185.

Lanza, F., Rohnacher, A., Janiszewski, H., & Wiemer, S. (2025). A large-N nodal array to study the structure and magmatic-tectonic processes of Kīlauea volcanic system. *EGU General Assembly*. https://doi.org/10.5194/egusphere-egu25-18464

Lin, G., Amelung, F., Lavallee, Y., & Okubo, P. G. (2014). Seismic evidence for a crustal magma reservoir beneath the upper east rift zone of Kilauea volcano, Hawaii. *Geology*, *42*(3), 187–190. https://doi.org/10.1130/g35001.1

Lin, G., Amelung, F., Shearer, P. M., & Okubo, P. G. (2015). Location and size of the shallow magma reservoir beneath Kīlauea caldera, constraints from near-source Vp/Vs ratios. *Geophysical Research Letters*, *42*(20), 8349–8357. https://doi.org/10.1002/2015gl065802

Lin, G., & Okubo, P. G. (2016). A large refined catalog of earthquake relocations and focal mechanisms for the Island of Hawai'i and its seismotectonic implications. *Journal of Geophysical Research*, *121*(7), 5031–5048. https://doi.org/10.1002/2016jb013042

Lin, G., & Okubo, P. G. (2020). Seismic evidence for a shallow detachment beneath Kīlauea's south flank during the 2018 activity. *Geophysical Research Letters*, *47*(15), e2020GL088003. https://doi.org/10.1029/2020gl088003

Lin, G., Roecker, S., Denlinger, R. P., O'Connell, D. R. H., Bennington, N., Vinarski, E., et al. (2026). Three-dimensional Vp, Vs, and Vp/Vs models of the summit of Kilauea, Hawai'i, from the 2023 Kilauea seismic imaging experiment [Dataset]. *Zenodo*. https://doi.org/10.5281/zenodo.22261306

Lin, G., & Shearer, P. M. (2007). Estimating local Vp/Vs ratios within similar earthquake clusters. *Bulletin of the Seismological Society of America*, *97*(2), 379–388. https://doi.org/10.1785/0120060115

Lin, G., & Shearer, P. M. (2021). Spatiotemporal variations of focal mechanism and in situ Vp/Vs ratio during the 2018 Kilauea eruption. *Geophysical Research Letters*, *48*(18), e2021GL094636. https://doi.org/10.1029/2021gl094636

Lin, G., Shearer, P. M., Amelung, F., & Okubo, P. G. (2015). Seismic tomography of compressional wave attenuation structure for Kīlauea volcano, Hawaii. *Journal of Geophysical Research*, *120*(4), 2510–2524. https://doi.org/10.1002/2014JB011594

Lin, G., Shearer, P. M., Hauksson, E., & Thurber, C. H. (2007). A three-dimensional crustal seismic velocity model for southern California from a composite event method. *Journal of Geophysical Research*, *112*(B11306). https://doi.org/10.1029/2007jb004977

Lin, G., Shearer, P. M., Matoza, R. S., Okubo, P. G., & Amelung, F. (2014). Three-dimensional seismic velocity structure of Mauna Loa and Kilauea volcanoes in Hawaii from local seismic tomography. *Journal of Geophysical Research*, *119*(5), 4377–4392. https://doi.org/10.1002/2013jb010820

Lin, G., & Thurber, C. H. (2012). Seismic velocity variations along the rupture zone of the 1989 Loma Prieta earthquake, California. *Journal of Geophysical Research*, *117*(B09301). https://doi.org/10.1029/2011jb009122

Lin, G., Thurber, C. H., Zhang, H., Hauksson, E., Shearer, P. M., Waldhauser, F., et al. (2010). A California statewide three-dimensional seismic velocity model from both absolute and differential times. *Bulletin of the Seismological Society of America*, *100*(1), 225–240. https://doi.org/10.1785/0120090028

Lo Bue, R., Rappisi, F., Firetto Carlino, M., Giampiccolo, E., Cocina, O., Vanderbeek, B. P., & Faccenda, M. (2024). Crustal structure of Etna volcano (Italy) from P-Wave anisotropic tomography. *Geophysical Research Letters*, *51*(13), e2024GL108733. https://doi.org/10.1029/2024gl108733

Matoza, R. S., Shearer, P. M., Lin, G., Wolfe, C. J., & Okubo, P. G. (2013). Systematic relocation of seismicity on Hawaii Island from 1992 to 2009 using waveform cross correlation and cluster analysis. *Journal of Geophysical Research*, *118*(5), 2275–2288. https://doi.org/10.1002/jgrb.50189

Monteiller, V., Got, J., Virieux, J., & Okubo, P. (2005). An efficient algorithm for double-difference tomography and location in heterogeneous media, with an application to the Kilauea volcano. *Journal of Geophysical Research*, *110*(B12), B12306. https://doi.org/10.1029/2004jb003466

Montgomery-Brown, E. K., Sinnett, D. K., Poland, M., Segall, P., Orr, T., Zebker, H., & Miklius, A. (2010). Geodetic evidence for enechelon dike emplacement and concurrent slow slip during the June 2007 intrusion and eruption at Kilauea volcano, Hawaii. *Journal of Geophysical Research*, *115*(B7), B07405. https://doi.org/10.1029/2009jb006658

Neal, C. A., Brantley, S. R., Antolik, L., Babb, J., Burgess, M., Calles, K., et al. (2019). The 2018 rift eruption and summit collapse of Kīlauea volcano. *Science*, *363*(6425), 367–374. https://doi.org/10.1126/science.aav7046

Nolet, G. (2008). *A breviary of seismic tomography: Imaging the interior of the Earth and Sun*. Cambridge University Press.

Okubo, P. G., Benz, H. M., & Chouet, B. A. (1997). Imaging the crustal magma sources beneath Mauna Loa and Kilauea volcanoes, Hawaii. *Geology*, *25*(10), 867–870. https://doi.org/10.1130/0091-7613(1997)025<0867:itcmsb>2.3.co;2

Okubo, P. G., & Wolfe, C. J. (2008). Swarms of similar long-period earthquakes in the mantle beneath Mauna Loa volcano. *Journal of Volcanology and Geothermal Research*, *178*(4), 787–794. https://doi.org/10.1016/j.jvolgeores.2008.09.007

Owen, S., Segall, P., Lisowski, M., Miklius, A., Denlinger, R., & Sako, M. (2000). Rapid deformation of Kilauea volcano: Global positioning system measurements between 1990 and 1996. *Journal of Geophysical Research*, *105*(B8), 18983–18998. https://doi.org/10.1029/2000jb900109

Park, J., Morgan, J. K., Zelt, C. A., & Okubo, P. G. (2009). Volcano-tectonic implications of 3-D velocity structures derived from joint active and passive source tomography of the island of Hawaii. *Journal of Geophysical Research*, *114*(B9), B09301. https://doi.org/10.1029/2008jb005929

Park, J., Morgan, J. K., Zelt, C. A., Okubo, P. G., Peters, L., & Benesh, N. (2007). Comparative velocity structure of active Hawaiian volcanoes from 3-D onshore-offshore seismic tomography. *Earth and Planetary Science Letters*, *259*(3–4), 500–516. https://doi.org/10.1016/j.epsl.2007.05.008

21699356, 2026, 10, Downloaded from https://agupubs.onlinelibrary.wiley.com/doi/10.1029/2026JB034515 by Capes, Wiley Online Library on [04/11/2026]. See the Terms and Conditions (https://onlinelibrary.wiley.com/terms-and-conditions) on Wiley Online Library for rules of use; OA articles are governed by the applicable Creative Commons License

Patrick, M., Johanson, I., Shea, T., & Waite, G. (2020). The historic events at Kīlauea volcano in 2018: Summit collapse, rift zone eruption, and Mw 6.9 earthquake: Preface to the special issue. *Bulletin of Volcanology*, *82*(6), 46. https://doi.org/10.1007/s00445-020-01377-5

Paulatto, M., Minshull, T. A., Baptie, B., Dean, S., Hammond, J. O. S., Henstock, T., et al. (2010). Upper crustal structure of an active volcano from refraction/reflection tomography, Montserrat, lesser Antilles. *Geophysical Journal International*, *180*(2), 685–696. https://doi.org/10.1111/j.1365-246x.2009.04445.x

Pavlis, G. L., & Booker, J. R. (1980). The mixed discrete-continuous inverse problem: Application to the simultaneous determination of earthquake hypocenters and velocity structure. *Journal of Geophysical Research*, *85*(B9), 4801–4810. https://doi.org/10.1029/jb085ib09p04801

Pisarenko, V. F., Kushnir, A. F., & Savin, I. V. (1987). Statistical adaptive algorithms for estimation of onset moments of seismic phases. *Physics of the Earth and Planetary Interiors*, *47*, 4–10. https://doi.org/10.1016/0031-9201(87)90062-8

Poland, M. P., Miklius, A., & Montgomery-Brown, E. K. (2014). Magma supply, storage, and transport at shield-stage Hawaiian volcanoes. *U.S. Geological Survey Professional Paper*, *1801*, 179–234.

Rawlinson, N., Pozgay, S., & Fishwick, S. (2010). Seismic tomography: A window into deep Earth. *Physics of the Earth and Planetary Interiors*, *178*(3–4), 101–135. https://doi.org/10.1016/j.pepi.2009.10.002

Riel, N., Kaus, B. J. P., Green, E. C. R., & Berlie, N. (2022). MAGEMin, an efficient gibbs energy minimizer: Application to igneous systems. *Geochemistry, Geophysics, Geosystems*, *23*(7), e2022GC010427. https://doi.org/10.1029/2022gc010427

Roecker, S., Denlinger, R. P., & O'Connell, D. R. H. (2026). Seismic catalogue derived from the 2023 Kilauea seismic imaging experiment, Kilauea, Hawai'i, USA [Dataset]. *U.S. Geological Survey data release*. https://doi.org/10.5066/P1WQ3UHP

Rowan, L., & Clayton, R. W. (1993). The three-dimensional structure of Kilauea volcano, Hawaii, from travel time tomography. *Journal of Geophysical Research*, *98*(B3), 4355–4375. https://doi.org/10.1029/92jb02531

Ryan, M. P. (1988). The mechanics and three-dimensional internal structure of active magmatic systems - Kilauea volcano, Hawaii. *Journal of Geophysical Research*, *93*(B5), 4213–4248.

Segall, P., Cervelli, P., Owen, S., Lisowski, M., & Miklius, A. (2001). Constraints on dike propagation from continuous GPS measurements. *Journal of Geophysical Research*, *106*(B9), 19301–19317. https://doi.org/10.1029/2001jb000229

Shalev, E., Kenedi, C. L., Malin, P., Voight, B., Miller, V., Hidayat, D., et al. (2010). Three-dimensional seismic velocity tomography of Montserrat from the SEA-CALIPSO offshore/onshore experiment. *Geophysical Research Letters*, *37*(19). https://doi.org/10.1029/2010gl042498

Spencer, C., & Gubbins, D. (1980). Travel-time inversion for simultaneous earthquake location and velocity structure determination in laterally varying media. *Geophysical Journal of the Royal Astronomical Society*, *63*(1), 95–116. https://doi.org/10.1111/j.1365-246x.1980.tb02612.x

Syracuse, E. M., Thurber, C. H., Wolfe, C. J., Okubo, P. G., Foster, J. H., & Brooks, B. A. (2010). High-resolution locations of triggered earthquakes and tomographic imaging of Kilauea Volcano's south flank. *Journal of Geophysical Research*, *115*(B10310). https://doi.org/10.1029/2010jb007554

Tanaka, S., Hamaguchi, H., Nishimura, T., Yamawaki, T., Ueki, S., Nakamichi, H., et al. (2002). Three-dimensional P-wave velocity structure of Iwate volcano, Japan from active seismic survey. *Geophysical Research Letters*, *29*(10), 59–1–59–4. https://doi.org/10.1029/2002gl014983

Thurber, C. (1984). Seismic detection of the summit magma complex of Kilauea volcano, Hawaii. *Science*, *223*(4632), 165–167. https://doi.org/10.1126/science.223.4632.165

Thurber, C., & Eberhart-Phillips, D. (2021). SIMUL codes for local earthquake tomography (version v1) [Software]. *Zenodo*. https://doi.org/10.5281/zenodo.5547889

Thurber, C., Roecker, S., Ellsworth, W., Chen, Y., Lutter, W., & Sessions, R. (1997). Two-dimensional seismic image of the San Andreas fault in the northern Gabilan range, central California: Evidence for fluids in the fault zone. *Geophysical Research Letters*, *24*(13), 1591–1594. https://doi.org/10.1029/97gl01435

Thurber, C. H. (1983). Earthquake locations and three-dimensional crustal structure in the Coyote Lake area, central California. *Journal of Geophysical Research*, *88*(B10), 8226–8236. https://doi.org/10.1029/jb088ib10p08226

Thurber, C. H. (1987). Seismic structure and tectonics of Kilauea volcano. *U.S. Geological Survey Professional Paper*, *1350*, 919–934.

Thurber, C. H. (1993). Local earthquake tomography: Velocities and Vp/Vs-theory. In H. M. Iyer & K. Hirahara (Eds.), *Seismic tomography: Theory and practice* (pp. 563–583). Chapman & Hall.

U.S. Geological Survey. (2023). Active and passive seismic interferometry of Kilauea volcano [Dataset]. *International Federation of Digital Seismograph Networks*. https://doi.org/10.7914/gqdb-hs97

Wadati, K., & Oki, S. (1933). On the travel time of earthquake waves. (Part II). *Journal of the Meteorological Society of Japan. Series II*, *11*(1), 14–28. https://doi.org/10.2151/jmsj1923.11.1_14

Wang, T., Zheng, Y., Pulvirenti, F., & Segall, P. (2021). Post-2018 Caldera collapse Re-Inflation uniquely constrains Kīlauea's magmatic System. *Journal of Geophysical Research*, *126*(6), e2021JB021803. https://doi.org/10.1029/2021jb021803

Wang, Y., Lin, F.-C., Schmandt, B., & Farrell, J. (2017). Ambient noise tomography across Mount St. Helens using a dense seismic array. *Journal of Geophysical Research*, *122*(6), 4492–4508. https://doi.org/10.1002/2016jb013769

Wegler, U., & Lühr, B. G. (2001). Scattering behaviour at Merapi volcano (Java) revealed from an active seismic experiment. *Geophysical Journal International*, *145*(3), 579–592. https://doi.org/10.1046/j.1365-246x.2001.01390.x

Wei, X., Shen, Y., Caplan-Auerbach, J., & Morgan, J. K. (2020). An OBS array to investigate offshore seismicity during the 2018 Kilauea eruption. *Seismological Research Letters*.

Wei, X., Shen, Y., & Morgan, J. K. (2023). Shallow volcano-tectonic structures on the Island of Hawai'i imaged by multimode Rayleigh wave ambient noise tomography. *Journal of Geophysical Research*, *128*(5), e2022JB026244. https://doi.org/10.1029/2022jb026244

Wessel, P., Luis, J. F., Uieda, L., Scharroo, R., Wobbe, F., Smith, W. H. F., & Tian, D. (2019). The generic mapping tools version 6 [Software]. *Zenodo*. https://doi.org/10.5281/zenodo.3407866

Wilding, J. D., Zhu, W., Ross, Z. E., & Jackson, J. M. (2023). The magmatic web beneath Hawaii. *Science*, *379*(6631), 462–468. https://doi.org/10.1126/science.ade5755

Wolfe, C., Okubo, P., Ekstrom, G., Nettles, M., & Shearer, P. (2004). Characteristics of deep (≥13 km) Hawaiian earthquakes and Hawaiian earthquakes west of 155.55 degrees W. *Geochemistry, Geophysics, Geosystems*, *5*, Q04006. https://doi.org/10.1029/2003GC000618

Wolfe, C. J., Solomon, S. C., Laske, G., Collins, J. A., Detrick, R. S., Orcutt, J. A., et al. (2009). Mantle shear-wave velocity structure beneath the Hawaiian hot spot. *Science*, *326*(5958), 1388–1390. https://doi.org/10.1126/science.1180165

Wu, S.-M., Huang, H.-H., Lin, F.-C., Farrell, J., & Schmandt, B. (2023). Extreme seismic anisotropy indicates shallow accumulation of magmatic sills beneath Yellowstone caldera. *Earth and Planetary Science Letters*, *616*, 118244. https://doi.org/10.1016/j.epsl.2023.118244

21699356, 2026, 10, Downloaded from https://agupubs.onlinelibrary.wiley.com/doi/10.1029/2026JB034515 by Capes, Wiley Online Library on [04/11/2026]. See the Terms and Conditions (https://onlinelibrary.wiley.com/terms-and-conditions) on Wiley Online Library for rules of use; OA articles are governed by the applicable Creative Commons License

Wu, S.-M., Lin, F.-C., Farrell, J., Shiro, B., Karlstrom, L., Okubo, P., & Koper, K. (2020). Spatiotemporal seismic structure variations associated with the 2018 Kilauea eruption based on temporary dense geophone arrays. *Geophysical Research Letters*, *47*(9), e2019GL086668. https://doi.org/10.1029/2019gl086668

Wu, S.-M., Lin, G., & Shearer, P. (2025). Seismic velocity monitoring reveals complex magma transport dynamics at Kīlauea Volcano prior to the 2018 eruption. *AGU Advances*, *6*(6), e2025AV001759. https://doi.org/10.1029/2025av001759

Yang, X., Lin, G., Bennington, N., & Gallant, E. (2026). Nodal seismic deployment on Mauna Loa Volcano, Hawaii: Dataset and preliminary insights. *Seismological Research Letters*, *97*(2A), 1215–1226. https://doi.org/10.1785/0220250232

Zandomeneghi, D., Aster, R., Kyle, P., Barclay, A., Chaput, J., & Knox, H. (2013). Internal structure of Erebus volcano, Antarctica imaged by high-resolution active-source seismic tomography and coda interferometry. *Journal of Geophysical Research*, *118*(3), 1067–1078. https://doi.org/10.1002/jgrb.50073

Zhu, W., & Beroza, G. C. (2019a). PhaseNet: A deep-neural-network-based seismic arrival-time picking method. *Geophysical Journal International*, *216*(1), 261–273.

Zhu, W., & Beroza, G. C. (2019b). PhaseNet: A deep-neural-network-based seismic arrival-time picking method [Software]. *AI4EPS*. https://github.com/AI4EPS/PhaseNet

Zollo, A., Gasparini, P., Virieux, J., le Meur, H., de Natale, G., Biella, G., et al. (1996). Seismic evidence for a low-velocity Zone in the upper crust beneath Mount Vesuvius. *Science*, *274*(5287), 592–594. https://doi.org/10.1126/science.274.5287.592

Zollo, A., Judenherc, S., Auger, E., D'Auria, L., Virieux, J., Capuano, P., et al. (2003). Evidence for the buried rim of Campi Flegrei caldera from 3-d active seismic imaging. *Geophysical Research Letters*, *30*(19). https://doi.org/10.1029/2003gl018173

21699356, 2026, 10, Downloaded from https://agupubs.onlinelibrary.wiley.com/doi/10.1029/2026JB034515 by Capes, Wiley Online Library on [04/11/2026]. See the Terms and Conditions (https://onlinelibrary.wiley.com/terms-and-conditions) on Wiley Online Library for rules of use; OA articles are governed by the applicable Creative Commons License